MASTER'S THESIS

CFD investigation of a unit cell inside a Plate Heat Exchanger

---

Author:

Mattias LY

Industrial Supervisor:

Erik ENGSTRÖM (Alfa Laval)

Co-Industrial Supervisor:

Gustav KARLSSON (Alfa Laval)

Academic Supervisor:

Prof. Christer FUREBY (LTH)

Examiner:

Prof. Christoffer NORBERG (LTH)

LUND UNIVERSITY

LTH, Faculty of Engineering

Department of Energy Sciences

Heat Transfer

June 12, 2023

Abstract

A numerical investigation of the unit cell approach has been done to reduce the computational cost for CFD (Computational Fluid Dynamics) of plate heat exchangers (PHE) at Alfa Laval. The reduced cost would enable LES (Large Eddy Simulation) to be done which would give a more detailed and accurate insight into the flow and heat transfer processes of the PHE. The unit cell which is repeatable in all directions is created by cutting out a small domain consisting of four contact points between the upper and lower plate of a full plate channel. Simulations of the unit cell have been done using LES in the software Ansys Fluent and compared with simulations of a whole plate done by Karlsson et al. [1]. The method of going from CAD (Computer Aided Design) to a CFD simulation of the unit cell has been developed and evaluated resulting in a recommendation regarding the method. It was found that the unit cell was able to capture the large-scale physics while the smaller scales were overpredicted. Taking this into consideration the method seems promising but still has room for improvement.

Popular Science Summary

The transport of heat from hot to cold mediums is called heat transfer. It can be used for either heating or cooling machines, electronics food, etc. in industry. Examples are the cooling of a car engine or recovering heat from a power plant turbine. In these types of applications, it is practical to use fluids of high heat capacity as mediums for transferring heat as this means they that they are to able carry more thermal energy per degree Kelvin. An effective way to transfer heat between hot and cold fluids is to use a plate heat exchanger (PHE). A PHE consists of multiple stacked plates that forms separate channels for the fluids which exchange heat between the thin plates. The corrugated geometry of the plates increases the surface area as well as the turbulence in the flow which both increases the heat transfer. An increasingly used tool in industry and in research to understand and visualize the complex flow as well as heat transfer processes is Computational Fluid Dynamics (CFD). The method uses computational power and numerics to solve these problems that are in most cases too complex to do by hand using empirical relations. Since the entire flow and heat transfer fields are solved in the simulated domain the post-processing possibilities are endless enabling the user to visualize the physics in 3D space as well as over time. However, doing a detailed simulation on a full plate of a heat exchanger would require vast computational resources. In an effort to reduce the computational cost this thesis investigates the idea of using a unit cell consisting of four contact points which could reduce the computational domain by factors of 100 or even thousand. This would enable the use of more accurate and detailed simulations within a reasonable time.

Acknowledgement

Contents

1 Introduction

1.1 Alfa Laval

This master's thesis is done in collaboration with Alfa Laval Technologies AB, a company with world leading competence within heat transfer, separation and fluid handling. The company provides many products worldwide that offer a broad range of industrial applications within mainly energy, environment, food and marine industry [2].

One of the products is the plate heat exchanger (PHE) which provides a compact and efficient way of transferring heat between two fluids compared to the shell and tube heat exchanger [3]. The fluids flow through separate channels formed by stacked thin corrugated plates that are sealed with gaskets and heat is transferred through the plates.

With the ongoing energy crisis and the constant work towards a more environmentally friendly society, new and improved technology within industry is needed. Improving the thermal efficiency of the PHE is therefore of great importance. In order to optimize heat transfer, computational fluid dynamics (CFD) is used to research and understand the flow and heat transfer processes in the PHE channels at Alfa Laval. The flow in these channels is complex and requires large computing power to simulate. An idea is therefore to use small periodic elements known as unit cells in order to reduce the computational cost which enables more detailed simulations to be done. A channel then consists of hundreds or even thousands of these unit cells.

1.2 CFD

The tool Computational Fluid Dynamics or CFD used for R&D at Alfa Laval, is a computer-based simulation method for solving fluid flow, heat transfer, and accompanying processes such as chemical reactions [4]. The method is based on the Navier-Stokes equations which are discretized and solved typically using RANS, LES, or DNS.

In Reynolds averaged Navier-Stokes (RANS), the instantaneous values in the Navier-Stokes equation are split into mean and fluctuating quantities using Reynolds decomposition. The mean flow is then solved while the fluctuating components describing the turbulence are modeled. This essentially means that all turbulence is modeled. RANS is the most widely used method in industry due to its robustness and low cost.

Another approach is Large Eddy Simulation (LES) where low-pass filtering is used to solve the larger scale energy-containing eddies and model the more universal smaller eddy scales. In doing so the turbulence and thus flow, heat transfer, and other involved

processes are more accurately captured compared to RANS. However, this comes at a greater computational cost since a time dimension is added where higher spatial and temporal resolutions are needed.

Direct Numerical Simulation (DNS) means that all turbulent scales are resolved since the Navier-Stokes equations are solved directly which gives the most accurate result since no modeling is needed. This becomes very computationally expensive because the majority of the computational resources are used to resolve the smallest turbulence scales [5]. Moreover, according to ANSYS FLUENT the cost of DNS is proportional to Re^3 at high turbulent Reynolds numbers [6] or $Re^{9/4}$ if the time scaling is also considered. This limits the use of DNS to simple canonical flows.

1.3 Problem Description and Objectives

The objective of this master thesis is to reduce the computational cost of CFD simulations by investigating if a unit cell accurately describes the flow and heat transfer inside a PHE channel. The cost of the unit cell is reduced by only simulating a fraction of the full plate computational domain. Moreover, simulations of the unit cell will be validated by quantitative and qualitative comparisons to simulations of mainly a whole plate done by Karlsson et al. [1] and experimental data by Focke et al. [7].
The reduction in computational power could enable the use of LES instead of RANS which would show a greater level of detail and could thus improve the research and development of PHE:s. Advantages and disadvantages will also be compared to the current method done on a full plate.
Lastly, a method from computer-aided design (CAD) to CFD simulation of a unit cell shall be developed.

The objectives for this work are:

- Develop a method for doing LES of a unit cell inside of PHE:s.

- Evaluate the level of detail and accuracy of the simulation results by comparisons with previous work of a full plate done by Karlsson et al. [1].

- Compare advantages and disadvantages of the unit cell method compared with the full plate method.

1.4 Benchmark

The full benchmark plate consists of 63 contact points with the dimensions 35 by 100 mm (see Figure 1). It should be noted that this geometry is very simplified making it a theoretical case. For example, the inlet and outlet ports are simplified in the form of rectangular ducts. Simulations were done in OpenFOAM using LES with resolutions approaching that of DNS. Moreover, RANS was also simulated [1].

The extensive work and different methods used in this case as well as its simplicity compared to a real plate channel is why it is chosen as a benchmark for evaluating this work.
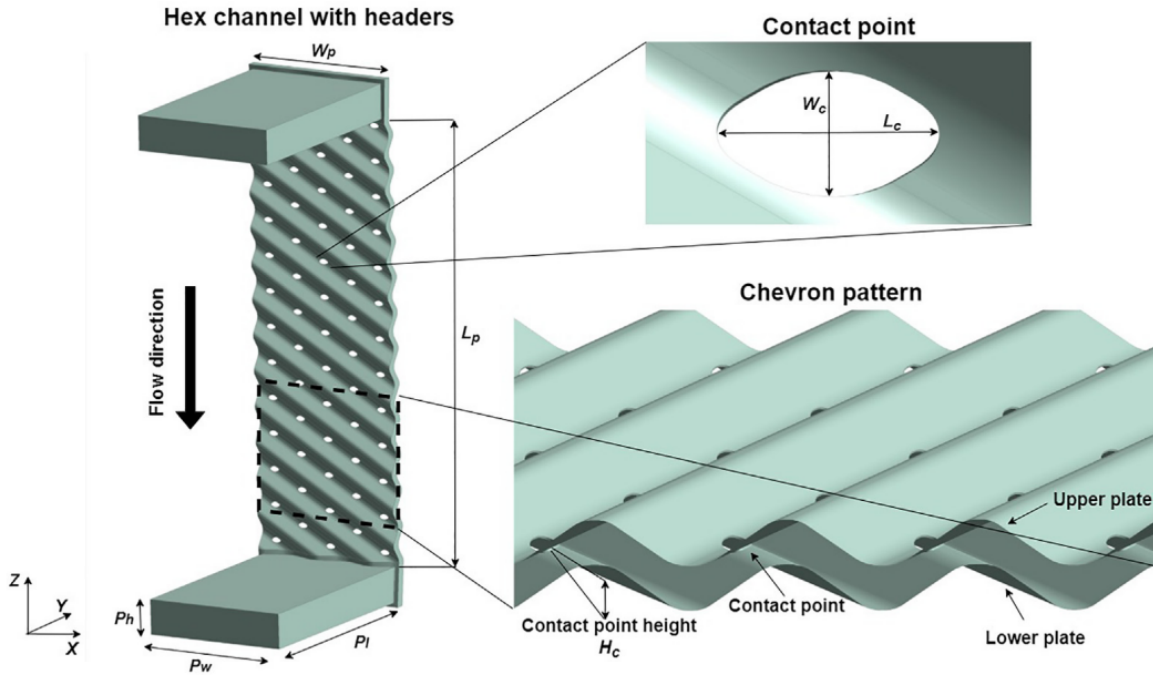
Figure 1: Full plate geometry with rectangular inlet and outlet ducts (reprinted with permission from Karlsson et al. [1]).

1.5 Geometry

The unit cell is created by cutting out a small piece of the full plate domain in figure 1. It should be a repeatable unit which means the smallest possible unit cell consists of four contact points (see fig.2). The fact that the four contact point is the smallest possible unit cell makes it particularly interesting to study in order to reduce the computational cost and understand its implications on the results. This is also why this work is based on the unit cell consisting of four contact points. Even though the unit cell is a simplified version of the industrial PHE there are still some challenging geometrical features to consider. To begin with, the corrugation angle is set to 60 degrees, and is defined as the angle between the corrugation and the main flow direction (see fig.2).

The interior domain representing the fluid channel is shown in figure 3. Since the unit cell is repeatable, a periodic length is defined as the distance between two end faces along one corrugation (see fig.4). The geometry of the plate corrugation itself is shown in fig.5. The contact points of the unit cell are of course identical to the ones of the full plate and thus shown in fig.1. Lastly, because of symmetry the upper and lower plates of the cell will have the same dimensions which are all presented in Table 1.
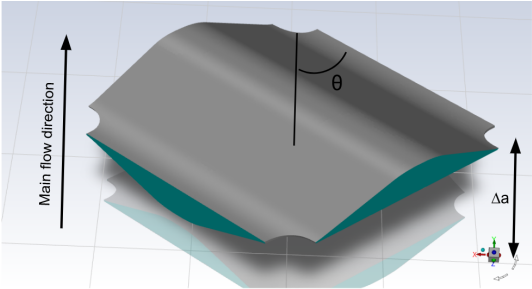
Figure 2: Unit cell geometry seen from bird eye-view where the two inlets are shown in green and the main flow direction is indicated by the black arrow. One quarter of the contact points are situated at each corner.
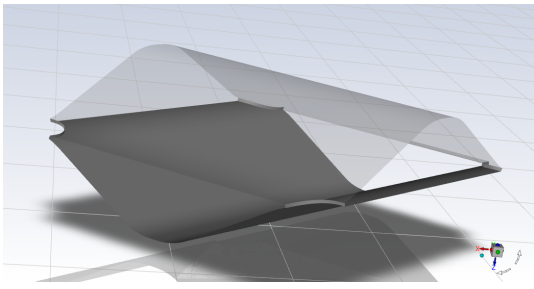
Figure 3: The upper plate has been made transparent displaying the interior geometry of the unit cell.
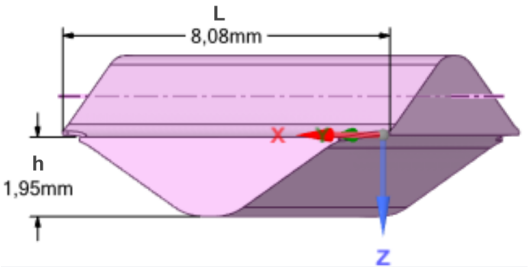
Figure 4: Periodic length L and mean channel height h.
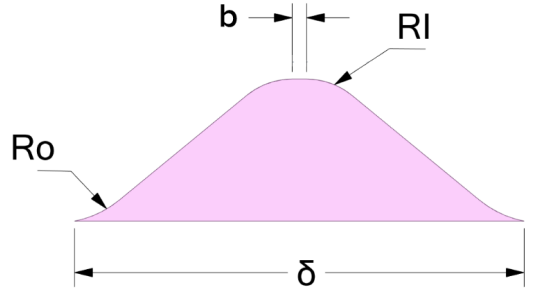
Figure 5: Upper beam width b, corrugation pitch δ, outer and inner radius R_o and R_I respectively. See Table 1 for values.

Table 1: Dimensions of the unit cell from figures 1 4 and 5.

Dimension	Value (mm)
Contact point height	$H_c = 0.1$
Contact point length	$L_c = 2.2$
Contact point width	$W_c = 1.25$
Corrugation pitch	$\delta = 7$
Inner radius	$R_I = 1.4$
Length of the unit cell	$\Delta a = 4.04$
Mean channel height	$h = 1.95$
Outer radius	$R_o = 1$
Periodic length	$L = 8.08$
Upper beam width	$b = 0.2$
Corrugation angle	$\theta = 60°$

2 Theory

2.1 Plate Heat Exchanger

In a Gasketed Plate Heat Exchanger (GPHE) the plates are pressed together by an external frame that is tightened with bolts. The channels formed between the plates are sealed with elastomeric gaskets which also directs the fluids into alternate channels [8]. Typically the fluids on each side of the plates flow in opposing directions i.e. in counterflow to increase the heat transfer efficiency (see fig.6).
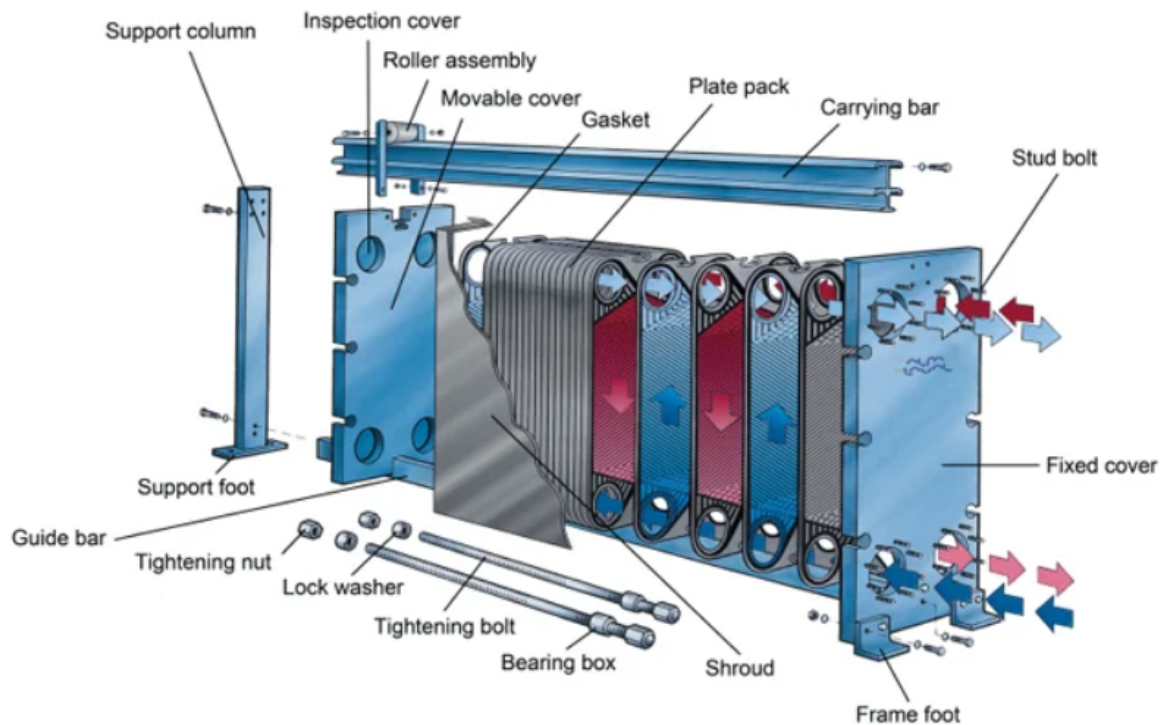
Figure 6: Full heat plate heat exchanger setup including the external frame. Counterflow is illustrated between hot (red) and cold (blue) fluids (reprinted from Alfa Laval [8]).

The standard plate pattern is the herringbone corrugation pattern. This pattern improves the heat transfer by increasing the heat transfer area. Moreover, the plates are stacked with the herringbone pattern in opposite directions which significantly increases the turbulent mixing and thus the heat transfer even further. Except for the herringbone patterned heat transfer area the plate also has round inlets or outlets at the corners followed by a "chocolate" patterned distribution which distributes the flow more evenly over the heat transfer area (see fig.7). This also reduces dead spots where the flow is slower allowing buildup of fouling or corrosion [9].
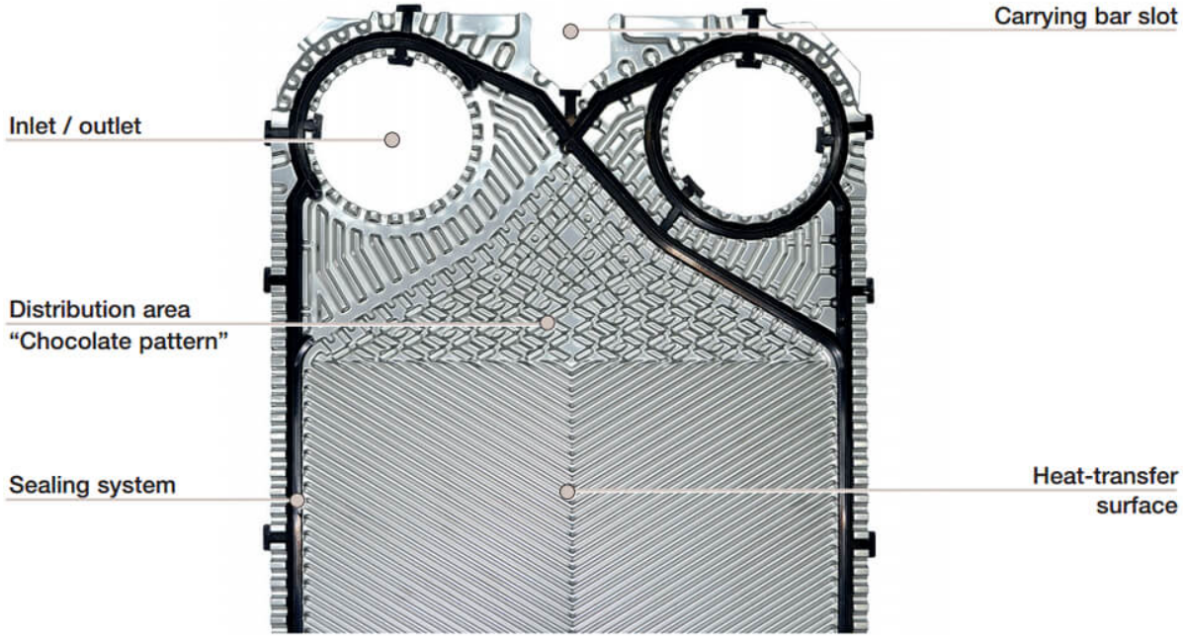
Figure 7: The chevron patterned plate with inlet, outlet and distribution area illustrated (reprinted from Alfa Laval [9]).

2.2 Flow and Heat Transfer Numbers

In this subsection the relevant numbers for quantifying the flow and heat transfer of this problem are presented. The Reynolds number Re is obtained using the following formula:

$$\text{Re} = \frac{\rho U_b D_h}{\mu} \tag{1}$$

where ρ is the fluid density (kg/m^3) and μ is the fluid viscosity (Pa s). U_b mean fluid bulk velocity (m/s) and the hydraulic diameter D_h (m) are defined as:

$$U_b = \frac{\int_{A_c} U dA}{A_c} \tag{2}$$

$$D_h = \frac{4A_c}{P_w} \tag{3}$$

where U is the mean velocity (m/s), A_c (m^2) is the cross-sectional area of the flow and P_w (m) is the wetted perimeter of the cross-sectional area. In order to stay consistent with the benchmark, the hydraulic diameter is approximated as the total channel height:

$$D_h \approx 2h \tag{4}$$

where h is the mean channel height (see Figure 4). The Fanning friction factor f_f and the Darcy friction factor f are calculated as:

$$f_f = \frac{|\Delta p| D_h / \phi}{\rho \Delta a \frac{U^2}{2}} \tag{5}$$

$$f = 4f_f \tag{6}$$

where Δp (Pa) is the pressure drop between the inlet and outlet faces, Δa (m) is the length of the unit cell in the main flow direction (see Figure 2) and ϕ is the surface enlargement factor defined as the ratio of the plate heat transfer area to its projected area on the xy-plane.

The Prandtl number, defined as the ratio of the momentum- to thermal diffusivity, can be obtained by the following formula:

$$\Pr = \frac{c_p \mu}{\kappa_f} \tag{7}$$

where c_p (J/K) is the specific heat capacity at constant pressure and κ_f (W/m K) is the thermal conductivity of the fluid.

By taking the ratio of the convective to the conductive heat transfer the Nusselts number is obtained:

$$\mathrm{Nu} = \frac{\alpha_1 D_h}{\kappa_f} \tag{8}$$

where α_1 (W/m^2 K) is the convective heat transfer coefficient inside the channel walls and is obtained using the following formulas:

$$Q = kA\Delta T_L \tag{9}$$

$$\frac{1}{k} = \frac{1}{\alpha_1} + \frac{1}{\alpha_2} + \frac{\delta}{\kappa_w} \tag{10}$$

$$\Rightarrow \alpha_1 = \frac{1}{\frac{A\Delta T_L}{Q} - \frac{1}{\alpha_2} - \frac{\delta}{\kappa_w}} \tag{11}$$

where A is the total heat transfer surface area, k is the total heat transfer coefficient, α_2 - convective heat transfer coefficient outside the channel, δ is the plate thickness and κ_w is the thermal conductivity of the plates. The logarithmic mean temperature difference for the unit cell can be calculated as [10]:

$$\Delta T_L = \frac{(T_\infty - T_{in}) - (T_\infty - T_{out})}{ln(\frac{T_\infty - T_{in}}{T_\infty - T_{out}})} \tag{12}$$

2.3 Governing Equations

The Navier-Stokes quations which governs the fluid flow and heat transfer processes for incompressible newtonian fluids excluding any source terms are as follows:

$$\frac{\partial u_i}{\partial x_i} = \mathbf{0} \tag{13}$$

$$\rho\frac{\partial u_i}{\partial t} + \rho\frac{\partial u_i u_j}{\partial x_j} = -\frac{\partial p}{\partial x_i} + \frac{\partial \sigma_{ij}}{\partial x_j} \tag{14}$$

$$\rho\frac{\partial e}{\partial t} + \rho\frac{\partial u_j e}{\partial x_j} = \sigma_{ij}\frac{\partial u_i}{\partial x_j} + \frac{\partial h_i}{\partial x_i} \tag{15}$$

where e (J/kg) is the internal energy and h_i is the heat flux vector (W/m^2):

$$e = \int c_V(T)dT \tag{16}$$

$$h_i = \kappa \nabla T \tag{17}$$

where κ is thermal conductivity (W/m K) and p (Pa) is the static pressure and σ_{ij} is the stress tensor of the fluid:

$$\sigma_{ij} = 2\mu S_{ij} - \lambda S_{kk}\delta_{ij} \tag{18}$$

where λ is the bulk viscosity (Pa s) using Stokes assumption [11]:

$$3\lambda + 2\mu = 0 \tag{19}$$

yields

$$\sigma_{ij} = 2\mu S_{ij} - \frac{2}{3}\mu S_{kk}\delta_{ij} \tag{20}$$

where S_{ij} is the strain rate tensor:

$$S_{ij} = \frac{1}{2}\left(\frac{\partial u_i}{\partial x_j} + \frac{\partial u_j}{\partial x_i}\right) \tag{21}$$

Equation 13 is the continuity equation which ensures that the mass is conserved. The second one is the momentum equation (eq.14) which establishes a momentum balance in all directions. The last equation is the energy equation (eq.15) which describes the energy transport of the flow [4].

2.4 Finite Volume Discretisation

The governing equations (eqs.13-15) stated in the previous subsection can be written in terms of a general transport equation for a generic variable Φ

$$\frac{\partial(\rho\Phi)}{\partial t} + \nabla \cdot (\rho\Phi\boldsymbol{u}) = \nabla \cdot (\Gamma \nabla \Phi) + S_\Phi \tag{22}$$

where Φ can be substituted by the transported variables (per unit volume) which are mass (ρ), momentum ($\rho\boldsymbol{u}$) and internal energy (e) respectively and the source term S_Φ is equal to zero. The respective terms in equation 22 have the physical according to the box below:

Rate of increase	Convection of ϕ	Rate of increase	Rate of increase
of Φ of fluid	+ out of fluid	= of Φ due to	+ of Φ due to
element	element	diffusion	sources

Integration of eq.22 over a control volume (**CV**) and a small time interval (Δt) gives [4]:

$$\int_t^{t+\Delta t} \frac{\partial}{\partial t}\left(\int_{CV} \rho\Phi dV\right)dt + \int_t^{t+\Delta t}\int_A \boldsymbol{n}\cdot(\rho\Phi\boldsymbol{u})dAdt = \int_t^{t+\Delta t}\int_A \boldsymbol{n}\cdot(\Gamma\nabla\Phi)dAdt + \int_t^{t+\Delta t}\int_{CV} S_\Phi dV dt$$

(23)

where Gauss's divergence theorem was used for the convection and diffusion terms:

$$\int_{CV}\nabla\cdot(\boldsymbol{a}) = \int_A \boldsymbol{n}\cdot\boldsymbol{a}dA$$

(24)

where $\boldsymbol{a}$ is an arbitrary vector and $\boldsymbol{n}$ is the normal vector to surface element dA. This enables the convective and diffusive flux terms to be discretized as sums of fluxes over the cell faces f with area ΔA. Performing the integrals over a cell with volume ΔV while assuming that Φ and S_Φ vary linearly within the cell yields:

$$\int_t^{t+\Delta t}\rho\frac{\partial\Phi_p}{\partial t}\Delta V dt = \int_t^{t+\Delta t}\sum_f(\Gamma\nabla\Phi\,\Delta\boldsymbol{A})_f - \sum_f(\rho\Phi\boldsymbol{u}\,\Delta\boldsymbol{A})_f\,dt + \int_t^{t+\Delta t}\overline{S}_\Phi\Delta V dt$$

(25)

where the values stored at the cell centers are denoted as Φ_p and the values at faces f are discretized in section 2.5.2. Tthe partial time derrivative is discretized and time integration is done in the following section 2.5.3 [11].

2.5   Discretization Schemes

2.5.1   Gradient Evaluation

In Fluent, gradients are used to calculate scalars at the cell faces and to evaluate the convection and diffusion terms of the discretized Navier Stokes equations. For this purpose, gradients are determined using the Least Squares Cell-Based Gradient Evaluation. This method assumes that the solution varies linearly between cell centers so that the change in value from cell $c0$ to its neighbor ci along direction vector δr_i can be written as:

$$(\nabla\Phi)_{c0}\cdot\Delta\boldsymbol{r}_i = (\Phi_{ci} - \Phi_{c0})$$

(26)

this can be expressed in matrix format to relate multiple cell centers:

$$[J](\nabla\Phi)_{c0} = \Delta\boldsymbol{\Phi}$$

(27)

where [J] is a function of the mesh geometry [6].

This linear system of equations is over-determined but can be solved by manipulating [J] using the Gram-Schmidt process [12] which yeilds:

$$\left(\frac{\partial \Phi}{\partial x}\right)_{c0} = \sum_{i=1}^{nb} W_{i0}^x \cdot (\Phi_{ci} - \Phi_{c0}) \tag{28}$$

$$\left(\frac{\partial \Phi}{\partial y}\right)_{c0} = \sum_{i=1}^{nb} W_{i0}^y \cdot (\Phi_{ci} - \Phi_{c0}) \tag{29}$$

$$\left(\frac{\partial \Phi}{\partial z}\right)_{c0} = \sum_{i=1}^{nb} W_{i0}^z \cdot (\Phi_{ci} - \Phi_{c0}) \tag{30}$$

where W_{a0}^b are weight factors and nb is the number of neighboring cells. The gradient can then be written in the following compact form [6]:

$$\nabla \Phi = \left(\frac{\partial \Phi}{\partial x_i}\right)_{c0} \tag{31}$$

2.5.2 Spatial Discretization

The gradients of the diffusion terms in equation 25 can be discretized using the Least Squares Cell-Based Gradient Evaluation directly (see subsection 2.5.1). However the convective terms are evaluated at the cell faces and need to be interpolated with care from the cell center values to ensure numerical stability and accuracy. To do this the following schemes implemented in FLUENT are used:

First order upwind

$$\Phi_{f,UP} = \Phi \tag{32}$$

Second order upwind

$$\Phi_{f,SOU} = \Phi + \nabla \Phi \cdot \vec{r} \tag{33}$$

Central differencing

$$\Phi_{f,CD} = \frac{1}{2}(\Phi_0 + \Phi_1) + \frac{1}{2}(\nabla \Phi_0 \cdot \vec{r_0} + \nabla \Phi_1 \cdot \vec{r_1}) \tag{34}$$

Given large enough Peclet numbers $\text{Pe} = \frac{\rho u}{\Gamma \delta x}$, the central differencing can result an in unbounded solution with non-physical wiggles that can lead numerical instability. The stability problem is resolved by using a implicit and explicit contribution to dampen the central differencing scheme:

$$\Phi_f^n = \Phi_{f,UP}^{n+1} + (\Phi_{f,CD}^n - \Phi_{f,UP}^n) \tag{35}$$

An alternative way of solving the instability problem that is used for this work is Bounded Central Differencing which is based on a normalized variable diagram (NVD) (for definition see B. P. Leonard [13]) and the convection boundedness criterion (CBC). Composed of central differencing, a central differencing and second order upwind blend, and first order upwind, the composite scheme is kept stable by using the these three schemes based on the NVD. Lastly, first order upwind is only used when the CBC is violated i.e. when the solution would get unbounded [6].

2.5.3 Temporal Discretization

In order to capture the time dependency of the problem with LES or URANS (Unsteady RANS), the temporal terms of the Navier Stokes equations need to be discretized. First order accuracy can be obtained if backward differencing is used to discretize the temporal term in equation 25:

$$\frac{\partial \Phi}{\partial t} \approx \frac{\Phi^{n+1} - \Phi^n}{\Delta t} = F(\Phi) \tag{36}$$

where $\mathbf{F}$ is a function including the spatial discretizations, n is the previous time step and $n+1$ is the next time step to be evaluated.

Here implicit time integration is used which means that the spatial function of the neighbouring cells $F(\Phi)$ is evaluated in the next time step $n+1$:

$$\frac{\Phi^{n+1} - \Phi^n}{\Delta t} = F(\Phi^{n+1}) \tag{37}$$

Now instead of backward differencing, Bounded Second-Order Implicit Time Integration is used for higher accuracy:

$$\frac{\partial \Phi}{\partial t} \approx \frac{\Phi^{n+1/2} - \Phi^{n-1/2}}{\Delta t} = F(\Phi^{n+1}) \tag{38}$$

Where the intermediate temporal quantities $\Phi^{n+1/2}$ and $\Phi^{n-1/2}$ are determined in the following way for a variable time step size:

$$\Phi^{n+1/2} = \Phi_n + (\tau\beta)^{n+1/2} \left(\Phi_n - \Phi^{n-1}\right) \tag{39}$$

$$\Phi^{n-1/2} = \Phi^{n-1} + (\tau\beta)^{n-1/2} \left(\Phi^{n-1} - \Phi^{n-2}\right) \tag{40}$$

Here β essentially serves as a weighting factor where the scheme becomes second-order when equal to one and first-order Euler backward if it is equal to zero. The time step size ratio τ is determined by [6]:

$$\tau^{n+\frac{1}{2}} = \frac{\Delta t^{n+1}}{(\Delta t^{n+1} + \Delta t^n)} \tag{41}$$

$$\tau^{n-\frac{1}{2}} = \frac{\Delta t^n}{(\Delta t^n + \Delta t^{n-1})} \tag{42}$$

12

which is a ratio designed to take into account that time levels that have large time step size between them should have more influence.

2.6 Pressure-Velocity Coupling

For incompressible flow the ideal gas law can no longer be used to couple the Navier Stoke's equations which leads to the velocity and pressure field becoming independent. This makes the need for a pressure-velocity coupling scheme since one equation is missing to close the system. In this work the PISO algorithm (by Issa 1986 [14]) is used to iteratively couple the pressure and velocity fields.
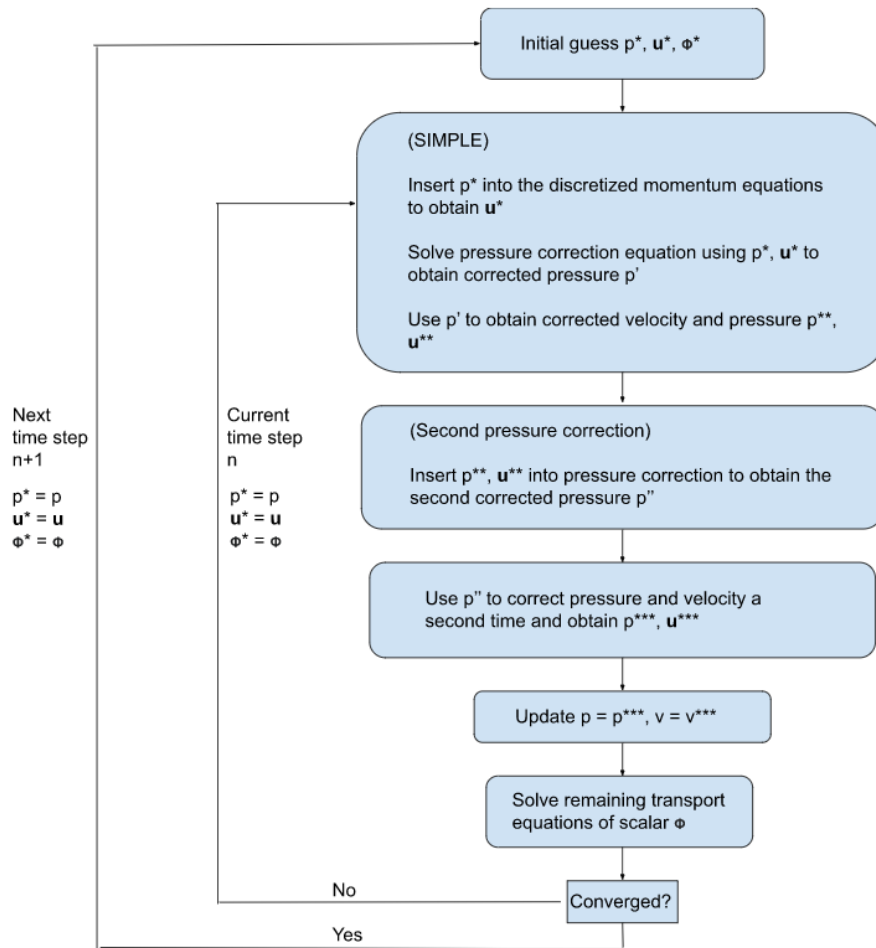

Figure 8: Schematics of the PISO algorithm when advancing from timestep n to n+1 (adapted from [4].

The steps in the PISO algorithm according to figure 8 are as follows [4]:

- An initially guessed pressure field is made.

- The algorithm uses a momentum predictor that calculates an initial velocity field from the momentum equations based on an initially guessed pressure field.

- Inserting the expressions for the pressure-corrected velocities into the continuity equation yields an equation for the pressure correction (as a function of initial velocities). This pressure correction is then used to correct the velocity and pressure field of the momentum predictor.

- The predicted velocity field is now inserted into the pressure correction equation to obtain a second pressure correction.

- The velocity and pressure fields from the predictor is then corrected a second time using the second pressure correction.

- The core set of variables are updated and the remaining equations are solved.

- The same procedure is done until the converges criteria are met after which a new time step is began.

2.7   RANS SST k-ω

The SST k-ω is a two equation eddy viscosity based RANS model. Like all RANS models it solves the mean flow of the Navier-Stokes equations and models the fluctuating components stored in the Reynolds stress tensor i.e turbulent contributions. The modeling is done by solving two equations and by using the eddy viscosity assumption (Boussinesq hypothesis). The two equations consist of one for the turbulent kinetic energy k and one for the turbulence frequency $\omega = \frac{k}{\epsilon}$. Additionally, the model is a blend of the $k - \omega$ model near to handle adverse pressure gradients and $k - \epsilon$ to model the free stream turbulence [4].

The RANS equation has the following form

$$\frac{\partial (\mathbf{U})}{\partial t} + \nabla \cdot (\mathbf{U} \otimes \mathbf{U}) = -\frac{1}{\rho}\nabla P + \nabla \cdot (\mathbf{S} - \mathbf{R}) \tag{43}$$

where $\mathbf{U}$ is the mean velocity vector and $\mathbf{R}$ is the Reynolds stress tensor defined as:

$$R_{ij} = <u_i' u_j'> \tag{44}$$

which is modeled using the Boussinesq hypothesis:

$$R_{ij} = \nu_t \left(\frac{\partial U_i}{\partial x_j} + \frac{\partial U_j}{\partial x_i} \right) - \frac{2}{3}\rho k \delta_{ij} \tag{45}$$

15

and the eddy viscosity is calculated as:

$$\nu_t = \frac{a_1 k}{max(a_1 \omega, \mathbf{S} F_2}$$

(46)

where a_1 is a constant, F2 is a blending function and $\mathbf{S} = \sqrt{(2S_{ij} S_{ij})}$. The turbulent frequency ω and turbulent kinetic energy are then calculated by a transport equation each:

$$\frac{\partial(\rho k)}{\partial t} + \nabla \cdot (\rho k \mathbf{U}) = \nabla \cdot \left[\left(\mu + \frac{\mu_t}{\sigma_k} \right) \nabla(k) \right] + \mathbf{P}_k - \beta^* \bar{\rho} \, k \, \omega$$

(47)

$$\frac{\partial(\rho \omega)}{\partial t} + \nabla \cdot (\rho \omega \mathbf{U}) = \nabla \cdot \left[\left(\mu + \frac{\mu_t}{\sigma_{\omega,1}} \right) \nabla(\omega) \right] + \gamma_2 \left(2 \rho \mathbf{S}_{ij} \cdot \mathbf{S}_{ij} - \frac{2}{3} \rho \omega \frac{\partial \mathbf{U}_i}{\partial x_j} \delta_{ij} \right) - \ldots$$

$$\beta_2 \rho \omega^2 + 2 \frac{\rho}{\sigma_{\omega,2} \omega} \frac{\partial k}{\partial x_k} \frac{\partial \omega}{\partial x_k}$$

(48)

where

$$\mathbf{P}_k = \left(2 \mu_t \mathbf{S}_{ij} \cdot \mathbf{S}_{ij} - \frac{2}{3} \rho \frac{\partial U_i}{\partial x_j} \delta_{ij} \right)$$

where μ is the dynamic viscosity, μ_t is the eddie viscosity and $\mathbf{S}_{ij}$ is the rate of deformation tensor. The remaining constants are shown below [4]:

Table 2: Coefficients for the SST $k - \omega$ model

σ_k	$\sigma_{\omega,1}$	$\sigma_{\omega,2}$	γ_2	β_2	β^*
1.0	2.0	1.17	0.44	0.083	0.09

2.8 LES Filtering

LES solves the largest scaled eddies by filtering away the smaller eddies (low-pass filtering). The filtering can be done in the wave or physical space. In Ansys Fluent space filtering (box filtering) is used in he following manner:

$$G\left(\boldsymbol{x}, \boldsymbol{x}'\right) = \begin{cases} 1/\mathrm{V}, & \boldsymbol{x}' \in \nu \\ 0, & \boldsymbol{x}' \text{ otherwise} \end{cases}$$

(49)

where V is the cell volume.

The filtered variables in the Navier Stokes equation can then be expressed as:

$$\overline{\Phi}\left(\boldsymbol{x}\right) = \int_D \Phi\left(\boldsymbol{x}'\right) G\left(\boldsymbol{x}, \boldsymbol{x}'\right) d\boldsymbol{x}'$$

(50)

where D is the fluid domain [6].

16

2.9 Filtered Navier-Stokes Equations

Applying the filter described in the previous section (subsection 2.8) to the incompressible Navier-Stokes equations (see eqs.13-15) with overbar notation for filtered quantities gives the corresponding equations for LES:

$$\frac{\partial \overline{u}_i}{\partial x_i} = \mathbf{0} \tag{51}$$

$$\rho \frac{\partial \overline{u}_i}{\partial t} + \rho \frac{\partial \overline{u}_i \overline{u}_j}{\partial x_j} = -\frac{\partial \overline{p}}{\partial x_i} + \frac{\partial \overline{\sigma}_{ij}}{\partial x_j} - \frac{\partial \tau_{ij}}{\partial x_j} \tag{52}$$

$$\rho \frac{\partial \overline{e}}{\partial t} + \rho \frac{\partial \overline{u}_j \overline{e}}{\partial x_j} = -\overline{p} \frac{\partial \overline{u}_i}{\partial x_i} + \overline{\sigma}_{ij} \frac{\partial \overline{u}_i}{\partial x_j} + \frac{\partial \overline{h}_i}{\partial x_i} - \frac{\partial q_i}{\partial x_i} \tag{53}$$

where the filtered stress tensor is:

$$\overline{\sigma}_{ij} \equiv \left[\mu \left(\frac{\partial \overline{u}_i}{\partial x_j} + \frac{\partial \overline{u}_j}{\partial x_i} \right) \right] - \frac{2}{3} \mu \frac{\partial \overline{u}_i}{\partial x_i} \delta_{ij} \tag{54}$$

and the subgrid-scale stress tensor τ_{ij} is defined as:

$$\tau_{ij} \equiv \rho \overline{u_i u_j} - \rho \overline{u}_i \overline{u}_j \tag{55}$$

The isotropic part of the subgrid-scale stress tensor τ_{kk} is added to the pressure term (or neglected for incompressible flows) while the deviatoric part need to be modeled for closure which will be shown in subsection 2.10. Moreover, the subgrid-scale heat flux vector is defined as:

$$q_j \equiv \rho \overline{u_i e} - \rho \overline{u}_i \overline{e} \tag{56}$$

and can be modeled in the following manner:

$$q_{ij} = -\frac{\mu_t}{\text{Pr}_t} \frac{\partial \overline{e}}{\partial x_j} \tag{57}$$

and Pr_t is the turbulent Prandtl number [6].

2.10 Wall-Adapting Local Eddy-Viscosity (WALE) Model

As discussed, the isotropic part of the subrid-scale stresses are not modeled, but added to the filtered static pressure term in Equation 52. The deviatoric part of the subrid-scale stress tensor which is unknown is modeled using the Smagorisky model:

$$\boldsymbol{\tau}_{ij} - \frac{1}{3} \boldsymbol{\tau}_{kk} \boldsymbol{\delta}_{ij} = 2\mu_t \left(\mathbf{S}_{ij} - \frac{1}{3} \mathbf{S}_{kk} \boldsymbol{\delta}_{ij} \right) \tag{58}$$

where τ_{ij} is the subgrid stress tensor defined in eq.55. Then the last unknown subgrid-scale turbulent viscosity is modeled using the WALE model [6]:

17

$$\mu_t = \rho L_s^2 \frac{(\mathbf{S}_{ij}^d \mathbf{S}_{ij}^d)^{3/2}}{(\overline{\mathbf{S}}_{ij}\overline{\mathbf{S}}_{ij})^{5/2} + (\mathbf{S}_{ij}^d \mathbf{S}_{ij}^d)^{5/4}} \tag{59}$$

$$L_s = min\left(\kappa d, C_w V^{1/3}\right) \tag{60}$$

$$\mathbf{S}_{ij}^d = \frac{1}{2}\left(\overline{\mathbf{g}}_{ij}^2 + \overline{\mathbf{g}}_{ji}^2\right) - \frac{1}{3}\boldsymbol{\delta}_{ij}\overline{\mathbf{g}}_{kk}^2, \;\; \overline{\mathbf{g}}_{ij} = \frac{\partial \overline{\mathbf{u}}_i}{\partial \mathbf{x}_j} \tag{61}$$

2.11 Wall Modeling

To treat the sharp gradients near the wall arising from the no-slip condition (zero tangential velocity at the wall) fluent uses a wall model which relates the non-dimensional filtered velocity $\overline{u}^+$ to a non-dimensional distance from the wall y^+:

$$\overline{u}^+ = \frac{\overline{u}}{u_\tau} \tag{62}$$

$$y^+ = \frac{\rho u_\tau y}{\mu} \tag{63}$$

where

$$u_\tau = \sqrt{\frac{\tau_w}{\rho}} \tag{64}$$

and τ_w is the wall shear stress. For low y^+ values when the centroid of the first cell layer is close to the wall in the viscous sublayer a linear relationship is used:

$$\overline{u}^+ = y^+ \tag{65}$$

If the mesh is coarser near the wall so that the y^+ values falls into the logarithmic region the law of the wall is used:

$$\overline{u}^+ = \frac{1}{\kappa}ln\left(Ey^+\right) \tag{66}$$

where $\kappa = 0.4187$ is the von Kármán constant and E = 9.793. For y^+ values in the buffer region a blend of the two relationships is used [6].

2.12 Lumley Triangle

One way to keep track of the characteristics of the anisotropic turbulence is by plotting the invariants of the normalized anisotropy tensor, which is based on the Reynolds stress tensor, in a so called Lumley triangle. Depending on where inside this triangle the invariants are located, different types of anisitropic turbulence can be determined and invariants outside the triangle corresponds to non-realizable Reynolds stress tensors. The invariants used are defined as:

$$6\eta^2 = -2II_b = b_{ii}^2 = b_{ij}b_{ji} \tag{67}$$

18

$$6\xi^3 = 3III_b = b_{ii}^3 = b_{ij}b_{jk}b_{ki} \tag{68}$$

where the normalized anisotropy tensor:

$$b_i j \equiv \frac{< u_i' u_j' >}{< u_k' u_k' >} - \frac{1}{3}\delta_{ij} = \frac{a_{ij}}{2k} \tag{69}$$

where angle brackets $< >$ denotes time average and k is the turbulent kinetic energy:

$$k = \frac{< u_k' u_k' >}{2} \tag{70}$$

where the fluctuating velocity component is obtained as:

$$u' = u - < u > \tag{71}$$

and a_{ij} is the anisotropic part of the Reynolds stress tensor [5]:

$$a_{ij} = R_{ij} - \frac{1}{3}R_{kk}\delta_{ij} \tag{72}$$

The different turbulent components inside the Lumley triangle are shown in figure 9.

Figure 9: The turbulent components inside the Lumley triangle (reprinted from Gao & Liu [15]).

2.13 Vorticity Equation

The rotating flow structures characterizing turbulence can be described using the vorticity vector defined as the curl of the velocity in the Cartesian tensor format:

$$\boldsymbol{\omega} = \nabla \times \boldsymbol{V} \tag{73}$$

By taking the curl of the incompressible Navier-Stokes equations (see eq.14), the following vorticity equation is obtained:

$$\frac{D\boldsymbol{\omega}}{Dt} = \nu\nabla^2\boldsymbol{\omega} + \omega \cdot \nabla\boldsymbol{u} \tag{74}$$

The first source term corresponds to viscous diffusion of the vorticicty while the second corresponds to vortex stretching which plays an essential role in the cascading of energy between eddie scales [5]. Together with the material derivative on the left hand side these terms describe the evolution or the transport of vorticity for incompressible flow.

2.14 Q-criterion

A way of visualizing vortical structures of CFD simulations is to plot the iso-surfaces of the so-called Q-criterion defined as [16]:

$$Q = \frac{1}{2}(\| \Omega_{ij}^2 \| - \| S_{ij}^2 \|) \tag{75}$$

where S_{ij} is the strain rate tensor previously defined (see eq.21) and Ω_{ij} is the vorticity tensor:

$$\Omega_{ij} = \frac{1}{2}\left(\frac{\partial u_i}{\partial x_j} - \frac{\partial u_j}{\partial x_i}\right) \tag{76}$$

Positive Q-values are obtained when the vorticity is dominating the over the strain thus indicating where vortex cores are present.

3 Modeling and Numerics

3.1 Boundary Conditions

Periodic mapping is done in two corrugation directions (see fig.10). The velocity at the outlet is then mapped to the corresponding periodic inlet to obtain a periodic flow:

$$\boldsymbol{u}(\vec{r} + \vec{L}) = \boldsymbol{u}(\vec{r} + \vec{L}) = \boldsymbol{u}(\vec{r} + 2\vec{L}) = ... \tag{77}$$

Due to viscous losses there will be a drop in pressure. The pressure is not a periodic quantity but the pressure drop can be seen as periodic:

$$\Delta p = p(\vec{r}) - p(\vec{r} + \vec{L}) = p(\vec{r} + \vec{L}) - p(\vec{r} + 2\vec{L}) = ... \tag{78}$$

The periodic velocity profile at the inlet is unknown, therefore a linearly varying pressure gradient β is set instead to drive the flow until the periodic feedback loop or mapping has developed it instead. The total pressure gradient is then decomposed in a linearly varying component $\beta \frac{\vec{L}}{|\vec{L}|}$ and a periodic quantity $\nabla \tilde{p}(\vec{r})$:

$$\nabla p(\vec{r}) = \beta \frac{\vec{L}}{|\vec{L}|} + \nabla \tilde{p}(\vec{r}) \tag{79}$$

where $\beta|\vec{r}|$ is the linearly varying pressure and $\tilde{p}(\vec{r})$ is the periodic pressure:

$$\tilde{p}(\vec{r}) = \tilde{p}(\vec{r} + \vec{L}) = \tilde{p}(\vec{r} + 2\vec{L}) = ... \tag{80}$$

Ideally the linearly varying pressure gradient would be set in the two periodic directions along respective corrugation. However only one direction for the pressure gradient was available in Fluent. Therefore the pressure gradient was set in the main flow direction (y-direction) to drive the desired mass flow which was iterated to fulfill the continuity equation (conservation of mass) in this direction (see fig.10).
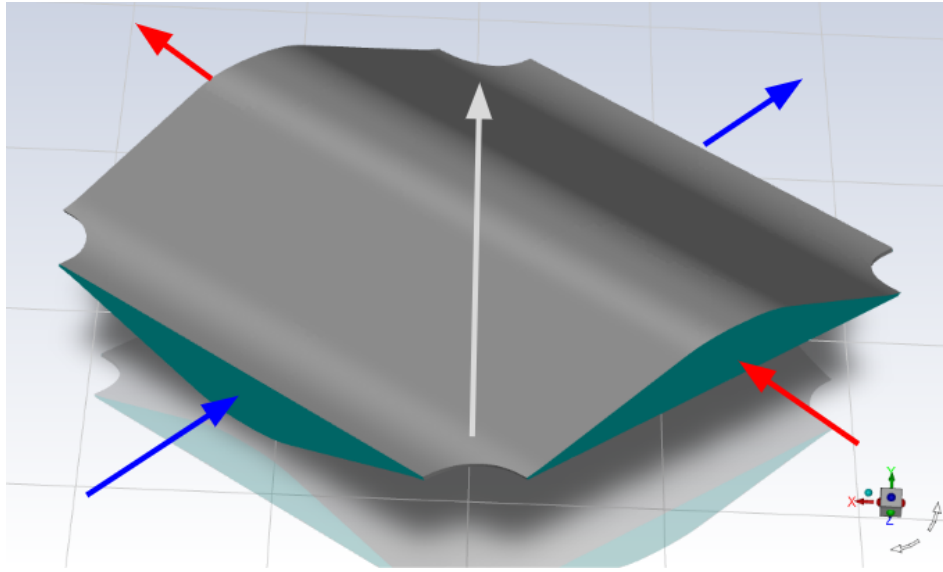
Figure 10: Illustration of the periodic boundary condition. Each of the periodic inlets of the cell are coupled to a periodic outlet creating two periodic directions indicated by the red and blue arrows respectively. The pressure gradient which drives the flow is set along the main flow direction marked by the grey arrow.

In an effort to align one of the periodic directions with the pressure gradient that could only be set in one direction, a unit cell consisting of five contact points was created (see fig.11). The idea was that using five contact points creates two new periodic directions one in the spanwise direction and one in the main flow direction. This would enabled the pressure gradient and the periodic direction in the main flow direction to align creating a more physically accurate boundary condition. This would also make it more intuitive to define the pressure drop and pressure gradient in of the unit cell since two periodic faces would be normal to the main flow direction. However this concept could not be used since the meshing tool Ansys Fluent Meshing with Watertight Geometry Workflow could not map the two periodic directions since they now collide due to being at the same height whereas previously one periodic direction bypassed under the second one. Another meshing tool could be used to mesh this geometry but this option was not used since the mesh would not be consistent with the benchmark which could affect the results.
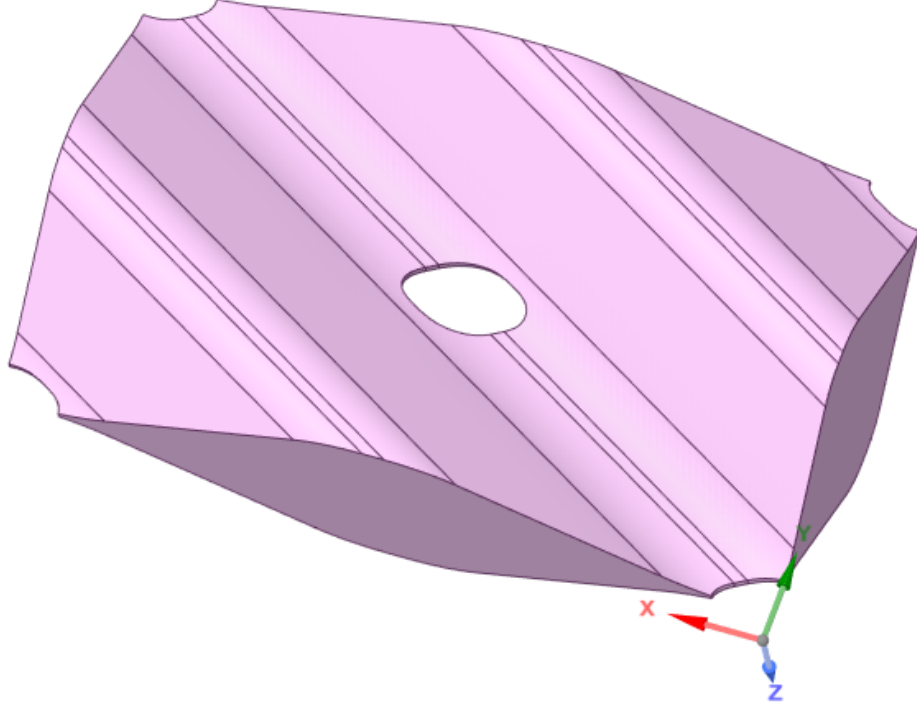
Figure 11: Conceptual unit cell consisting of five contact points which creates periodic faces normal to the spanwise direction (x) and the main flow direction (y).

Convective boundary conditions are set at the walls except for the contact points which are assumed to be adiabatic. Additionally, an artificial thickness δ together with a thermal conductivity is added to the heat transferring walls in order to take heat conduction of the plate into account. The Ansys Fluent users's guide recommends either constant temperature or heat flux for periodic heat transfer which is why this is not well documented for the convective condition. However the convective boundary condition is still chosen since it represents the heat transfer of the PHE most realistically. Therefore, it can only be speculated how this would be done in Fluent. It seems possible that the periodic heat transfer is solved by mapping the temperature similar to how the velocity was solved but for the temperature profile instead of the actual temperature since it would continuously increase until wall temperature due to thermal equilibrium. Treating the temperature profile φ as a periodic quantity it can be expressed as:

$$\boldsymbol{\varphi}(\vec{r}+\vec{L}) = \boldsymbol{\varphi}(\vec{r}+\vec{L}) = \boldsymbol{\varphi}(\vec{r}+2\vec{L}) = ... \tag{81}$$

where

$$\varphi = \frac{T - T_\infty}{T_{b,in} - T_\infty} \tag{82}$$

by doing this the outlet temperature profile can be mapped to the inlet thus fullfilling the periodicity. In order to prevent the temperature from increasing to the wall temperature, the temperature profile at the inlet can simply be rescaled to maintain the

23

specified bulk inlet temperature after each iteration. The thermal boundary conditions discussed are condensed into table 3.

Table 3: The thermal boundary conditions summarised.

Boundary	Inlet	Outlet	Contact point	Upper wall	Lower wall
Condition	Periodic	Periodic	Adiabatic	Convection	Convection
Value	$T_{b,in} = 293.15$ K	-	$q = 0$	$T_{inf} = 333$ K	$T_{inf} = 333$ K

Finally, smooth wall condition is used and no-slip condition is applied at the wall which means that the tangential fluid velocity is zero at the wall. The fluid used is water and all properties can be seen in Table 4.

Table 4: Fluid and solid properties of the unit cell.

Property	Value
Thermal conductivity	$\kappa = 0.09$ W/m K
Thermal wall conductivity	$\kappa_w = 15$ W/m K
Density	$\rho = 998.2$ kg/m^3
Specific heat capacity	$c_p = 712$ J/kg
Dynamic viscosity	$\mu = 1 \cdot 10^{-3}$ kg/m s
Convective heat transfer coefficient	$\alpha_2 = 20\,000$ W/m^2 K
Virtual plate thickness	$\delta = 0.3$ mm
Heat capacity ratio	$\gamma = 1$
Turbulent Prandtl number	$\mathrm{Pr}_t = 0.7$

3.2   Assumptions

The boundary conditions are simplifications of the real problem and makes it possible to implement and solve it in a computer program. Due to the complexity of the physics involved in reality even further simplifications or assumptions are needed to be able to handle the problem at a reasonable level. The assumptions used are therefore the following:

- No fouling at wall surfaces since this operation condition is not needed for the evaluation of the designed heat transfer.

- Shape of contact points assumed to form uniform ellipses with chamfers in order to get a good mesh.

- Uniform plate thickness is assumed whereas in reality the thickness will vary due to the manufacturing process where the plate shape is pressed with tools.

- Isotropic and homogeneous thermal properties of walls even though pressing can cause anisotropy and the material itself could have defects.

- Fully developed flow due to the translational periodic condition which mimics a flow domain of infinite length, no inlet and outlet effects.

- Effects of end walls are disregarded since the periodic domain can be seen as having an infinite width.

- Negligible gravity and Buoyancy forces are excluded.

- No conjugate heat transfer, the ambient environment outside the plate channels are treated as a constant temperature heat source. The simplified heat problem is deemed sufficient to evaluate the heat transfer performance of the unit cell. Otherwise the problem would become to complex and expensive which would take away focus on the main objective.

- Thermal radiation is negligible at the relatively low temperatures used.

3.3 Numerical Setup

The settings and motivations for the numerical schemes used to solve the problem are presented here and the theory behind them were previously presented in the theory section (see section 2).

- Simulation type: LES which is chosen because it gives detailed results which will help the evaluation of the unit cell method. LES was also chosen to see if it works well with the unit cell setup from a accuracy and a computational cost stand point since one of the aspirations with the unit cell method is that the reduced cost will enable LES to be used.

- Subgrid-scale model: Wall-Adapting Local Eddy-Viscosity (WALE) is used to account for strain and rotations of the smallest sub-grid scale eddies. Another advantage is that the subgrid-scale model produces the correct asymptotic wall behavior ($\nu_t = O(y^3)$) [17]. If implemented correctly these properties should make the model suitable for the current wall-bounded flow problem where large rotations are created due to the geometry as well as large strains due to impingement.

This model was also used by the benchmark which will make the comparison more direct.

- Pressure-Velocity Coupling: Pressure-Implicit with Splitting of Operators (PISO). This scheme was chosen to reduce the large number of iterations required for convergence associated with transient simulations [6].

- Mass Flux: Rhie-Chow: distance based (interpolation) to prevent checkerboard oscillations [4].

- Gradient evaluation: Least Squares Cell Based gradient is chosen because it is better than the cell based gradient and has similar accuracy to the node based gradient at a lower cost for skewed meshes [6].

- Pressure: Second Order Central Differencing of the pressure is good for handling swirling flow while maintaining second order accuracy [6]. This is suitable for this problem which has a swirling nature and require higher accuracy due to LES being used.

- Momentum: Bounded Central Differencing For higher order spatial accuracy required for LES while maintaining stability [6].

- Energy: Second Order Upwind (default) [6].

- Transient Formulation: Bounded Second Order Implicit is chosen to handle the transient term of Equation 25 for improved temporal accuracy and stability [6].

3.4 Procedure

- The finest mesh was ran to 20 flow through times (t_f) to ensure convergence. The flow through time here is the time taken for the bulk flow to pass through the entire domain once.

- Convergence quantities where mean (over time) pressure, velocity and temperature averaged over a vertical line through the center of the cell domain (see fig.25) as well as the total mass flow rate in the main flow direction and the Fanning friction factor.

- The $20t_f$ solution file was used as an initial condition for the following simulations of all three meshes where a transition time of $5t_f$ was used after which sampling began for $50t_f$.

- CFL based adaptive time stepping is used to control the time step size and keep stability and temporal accuracy. Where the Courant number is defined as $CFL = \frac{U\Delta t}{\Delta x}$ and Δx is the grid spacing.

Table 5: Time advancement and sampling configuration.

Time parameter	Value
Courant–Friedrichs–Lewy number	$\text{CFL} = 1$
Flow through time	$t_f = 0.033$ s
Initial time	$t_i = 20t_f$ s
Transition time	$t_t = 5t_f$ s
Sampling time	$t_s = 50t_f$ s

3.5 CAD to CFD

The method for setting up a simulation of the unit cell is as follows:

- Import plate CAD geometry into Spaceclaim.

- Cut out a unit cell from the geometry and name the periodic inlet and outlet patches.

- Export the unit cell CAD geometry into Ansys Fluent Meshing with Watertight Geometry Workflow.

- Generate a surface mesh.

- Map each periodic face/patch pair using the option: boundary -> recover periodic -> translational and set the correct offset between the periodic faces.

- After this inflation layers and volume mesh are set up and generated.

- The mesh is then imported into Fluent and the necessary boundary conditions and numerics are set according to previous subsections (see subsection 3.1 and subsection 3.3) after which the case is ready to be simulated.

3.6 Mesh Convergence Study

To ensure that the results are not affected by the mesh size a mesh study of the flow and heat transfer has been conducted. The meshes are done in the same meshing program with the same settings as the benchmark for consistency. A total of three mesh sizes or cell counts have been included in the study: 60k, 140k and 250k cells. These meshes correspond to 3M, 11M and 45M cells respectively of the benchmark. The meshes are shown on a slice cut through two contact points normal to the main flow direction in figure 12.
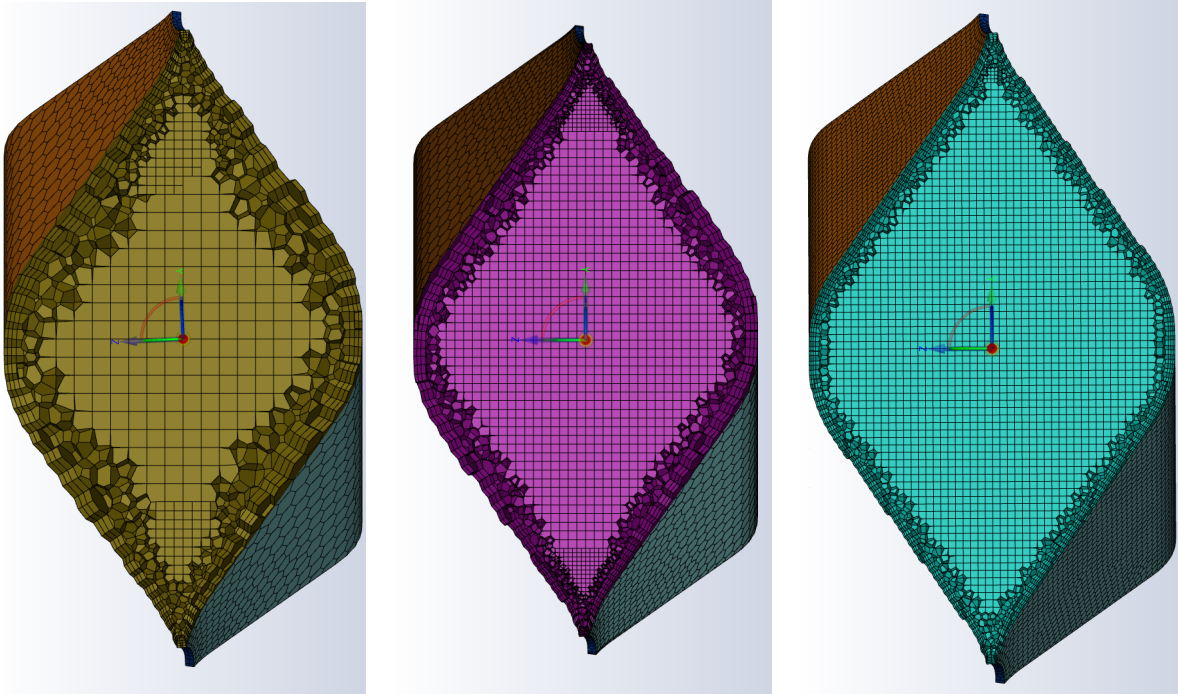
Figure 12: Mesh sizes of 60k, 140k and 250k cells are shown in sequential order from left to right.

The meshes used are of type poly hex-core which combines poly cells with hexahedral cells at the core of the domain. All meshes use 3 inflation layers to capture sharp gradients of the near wall flow and structured hexahedral mesh at the core to improve accuracy by improving element quality reducing interpolation errors between cells. Polyhedral cells are used as a buffer to transition from the inflation layer to the hexahedral cells. The y^+ values which indicates the near wall resolution are shown in Table 6.

It is expected that the discretization error will decrease asymptotically as finer and finer elements are used. The goal of the mesh convergence study is then to find a mesh size where the solution is adequately independent of the size. However in this case it is observed that the asymptotic behavior is missing in figures 14, 15 and 16 but seems promising for the velocity in figure 13.

28

Table 6: y^+ values for the unit cell meshes and for the respective mesh sizes of the full plate.

Unit Cell Mesh	min y^+	max y^+	avg. y^+
60k	0.0843	3.8	1.19
140k	0.0409	3.42	1.02
250k	0.0665	1.73	0.68
Full Plate Mesh			
3M	0.0192	8.39	2.07
11M	0.0043	6.02	1.71
45M	0.0006	3.19	0.96
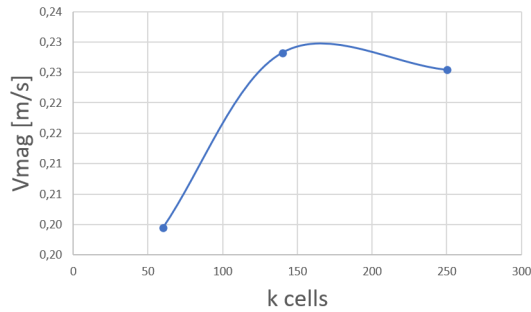
Figure 13: Mean velocity average over the vertical probe (see fig.25).
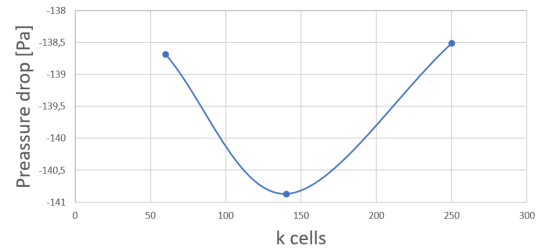
Figure 14: Mean pressure drop between inlet and outlet faces.
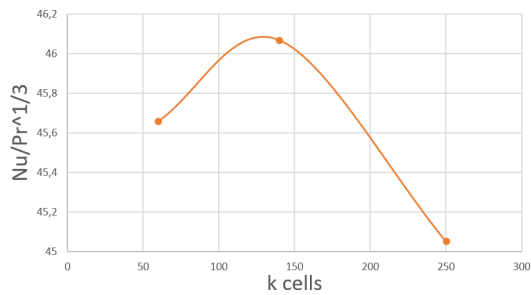
Figure 15: Mean $Nu/Pr^{1/3}$.
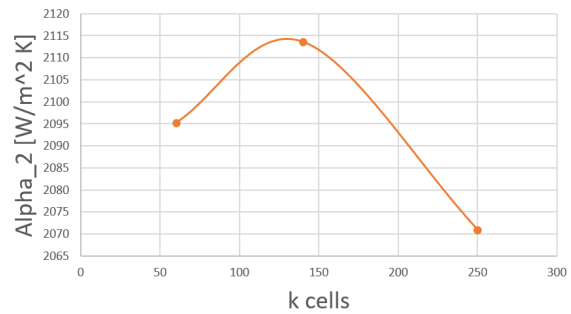
Figure 16: Mean convective heat transfer coefficient α_2.

4 Results and Discussion

In this section the results of the unit cell simulations are presented. First the obtained fields and profiles will be shown of both the unit cell and the whole plate for comparisons to be made. In the following subsection the Darcy friction factor and $\mathrm{Nu}/\mathrm{Pr}^{1/3}$ are plotted against data from the full plate and experiments. After that the unit cell results from RANS, URANS and LES for different mesh resolutions are displayed. Next, the anisotropy of turbulence in the unit cell is shown in the Lumley triangle followed by the wake and vortex structures and lastly the sources of errors are discussed.

4.1 Comparison with Full Plate

4.1.1 Velocity Field

The instantaneous, mean and fluctuating velocity fields are shown through different sections of both the unit cell and the full plate. First a slice taken at the middle of the channel height of the full plate is shown in figure 17. The same plate is then cut out into the same shape as a unit cell in figure 18 where it is directly compared to the actual unit cell. The same thing as figure 18 is shown in figure 19 but through a slice normal to the mean flow direction instead. Note that the cutouts of the full plate are done in the middle centre part of the plate since this is where the flow would be most developed and thus give the best comparison with the unit cell.
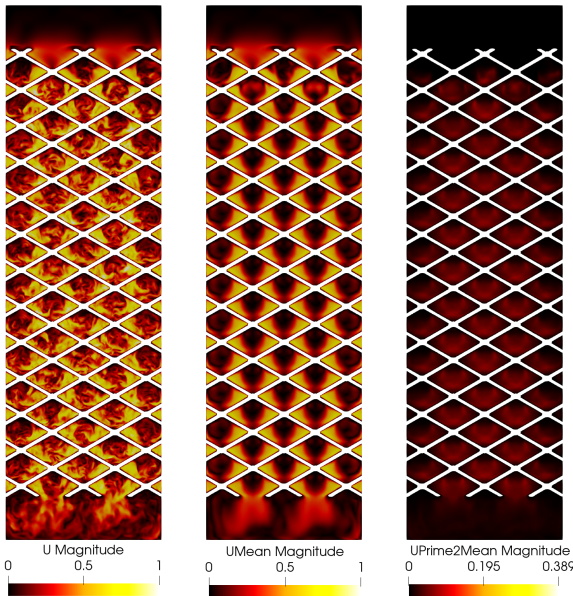

Figure 17: The velocity field of the full plate is shown in terms of instantaneous (left), mean (middle) and root-square mean of fluctuating (right) velocity magnitudes respectively.
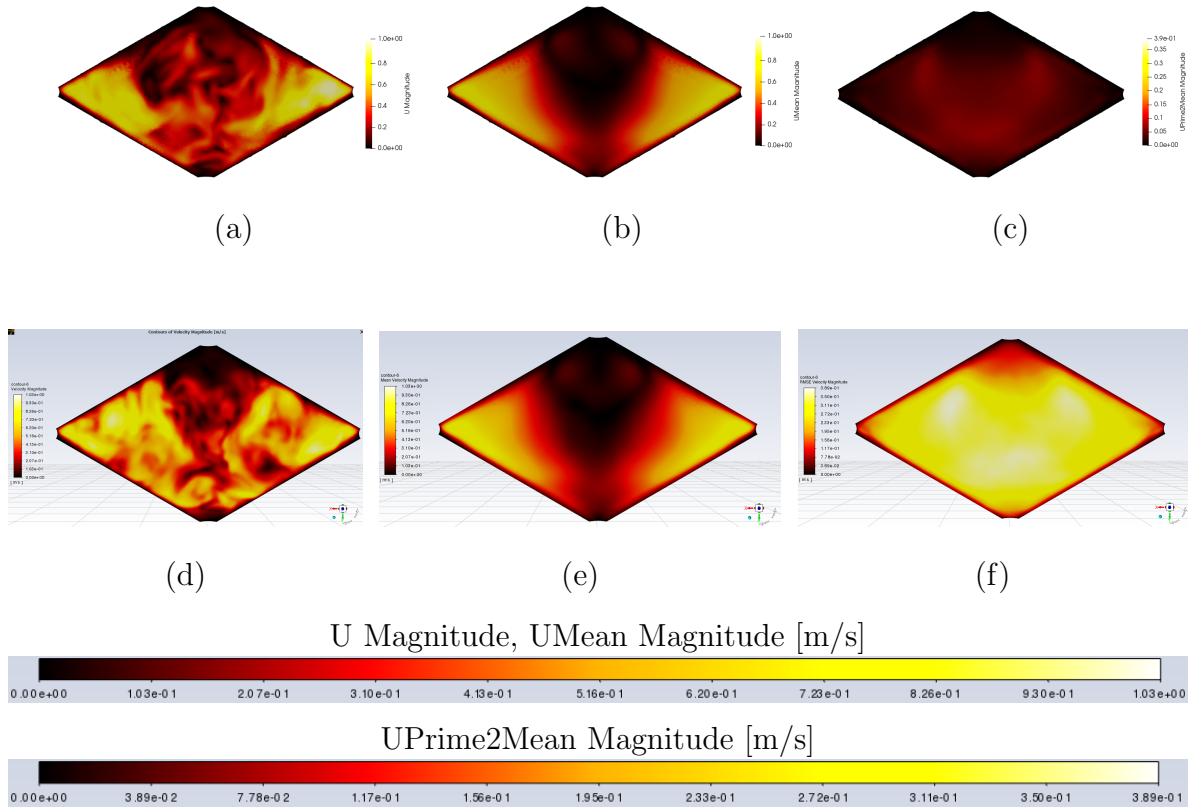
Figure 18: The velocity field of the full plate (upper) and the unit cell (lower) is shown in terms of instantaneous (a,d), mean (b,e) and root-square mean of fluctuating (c,f) velocity magnitudes respectively. The velocities are shown in a mid-plane at half the channel height.
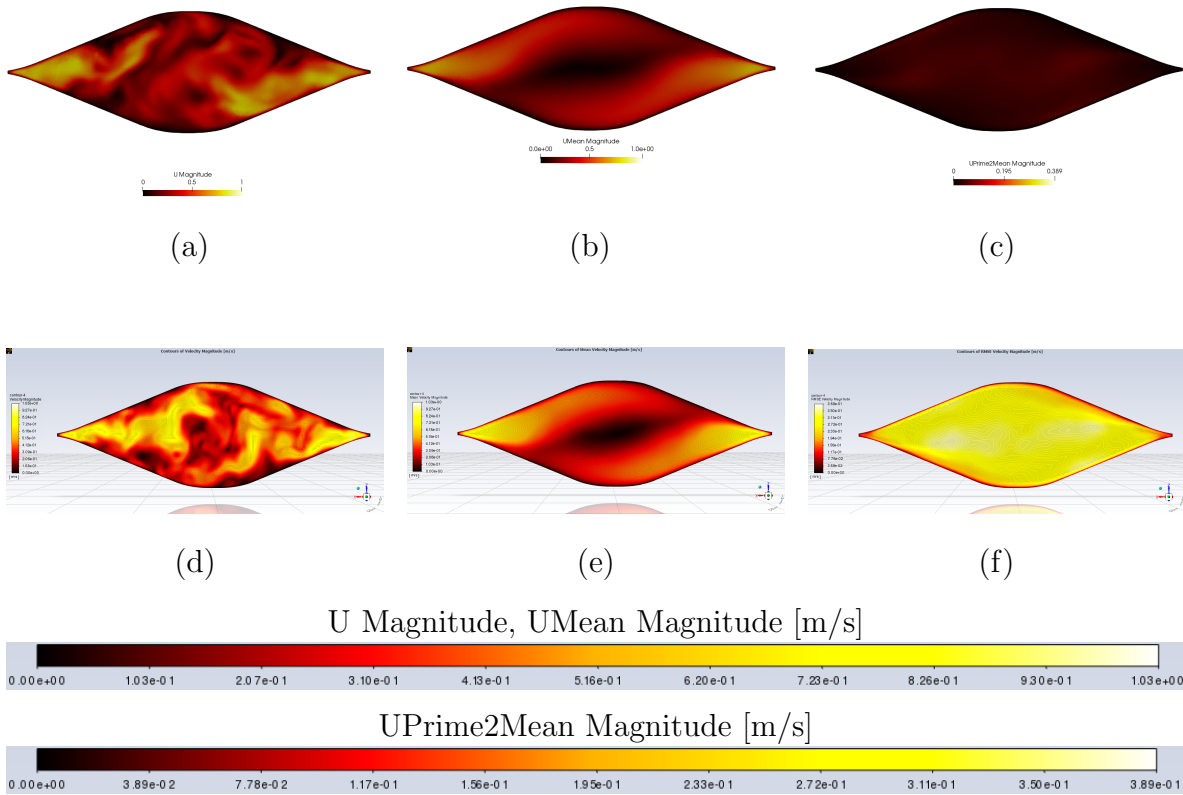
Figure 19: The velocity field of the full plate (upper) and the unit cell (lower) is shown in terms of instantaneous (a,d), mean (b,e) and root-square mean of fluctuating (c,f) velocity magnitudes respectively. The velocities are shown in plane which is cut through two contact points normal to the mean flow direction.
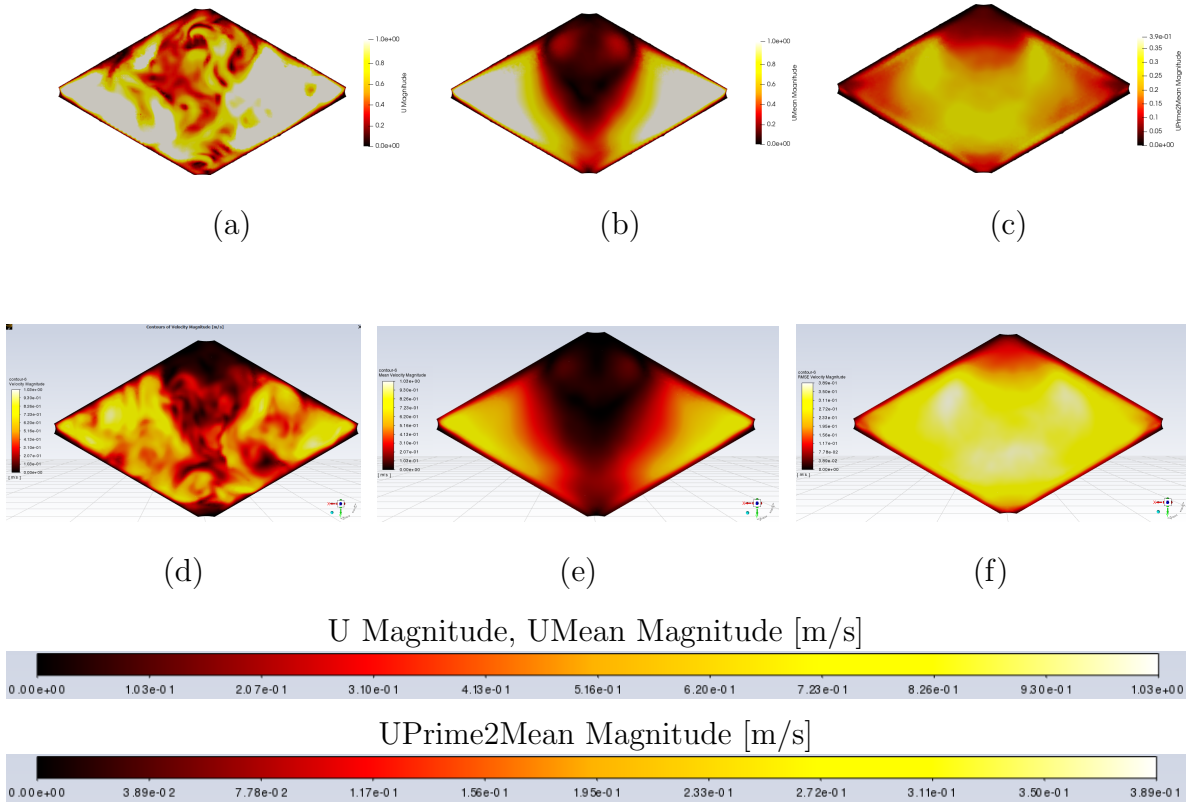
Figure 20: The velocity field of the full plate for Re = 1273 (upper) and the unit cell for Re = 841 (lower) is shown in terms of instantaneous (a,d), mean (b,e) and root-square mean of fluctuating (c,f) velocity magnitudes respectively. The velocities are shown in a mid-plane at half the channel height.

The velocity field seems to agree with the benchmark showing higher velocities around the side of the contact points. This is probably due to the flow not following the corrugations but instead reflects into the opposite corrugation direction due to the high chevron angle [18]. The back and fourth reflection would then form a helix structure that goes between the contact points shifting between upper and lower corrugation in the direction of the mean flow causing the high velocity between the contact points. Acceleration of the flow around the sides of the contact points due to their curvature is probably also a contributing factor to this. Therefore it seems that the velocity field is captured qualitatively when looking at the mean and instantaneous ones (see figures 18 and 19). For the instantaneous velocity, the characteristics and dynamics look similar where vortex shedding seems to be captured at the sides of the contact points. It can be seen from the same figures that low velocity regions are observed at the stagnation point in front of the contact point and in the wake region behind it which seems to be well captured. Interestingly the root square mean of the fluctuating velocity field also have the same contour but is largely overpredicted by an order of ten (see figures 18 and 19).

4.1.2 Wall Shear Stress & Heat Flux

The shear stress and heat flux on the walls of the unit cell and full plate are shown in figures 21-22 and figures 23-24 respectively.
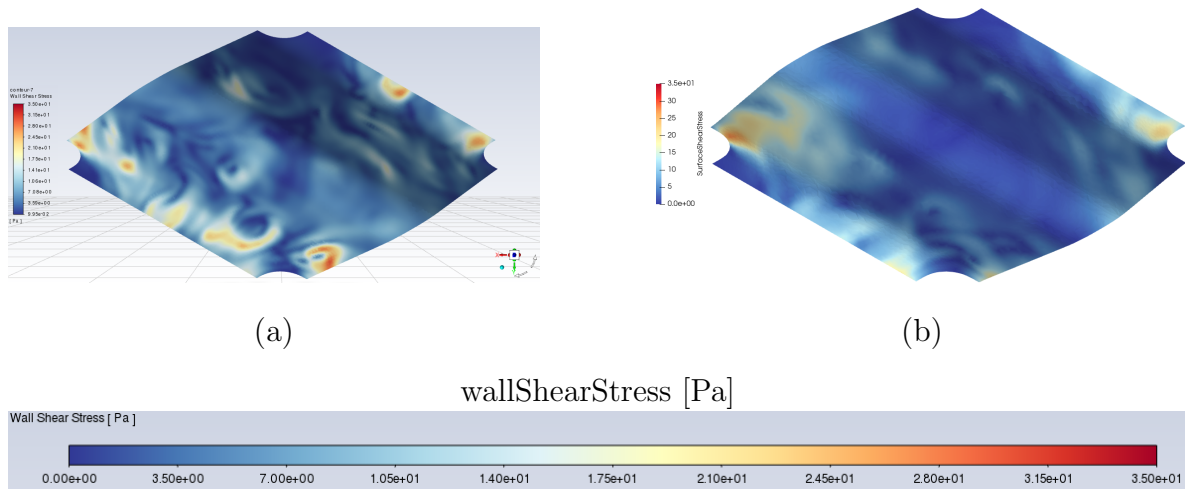

(a)

(b)

wallShearStress [Pa]

Figure 21: Instantaneous wall shear stress of the upper plate for the unit cell (left) and the full plate (right).

(a)

(b)

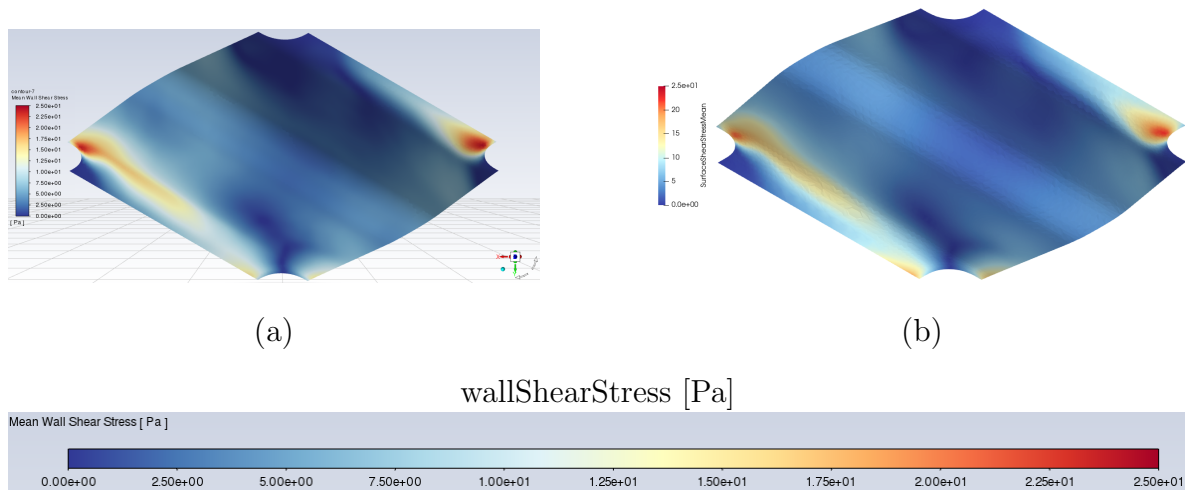wallShearStress [Pa]

Figure 22: Mean wall shear stress of the upper plate for the unit cell (left) and the full plate (right).
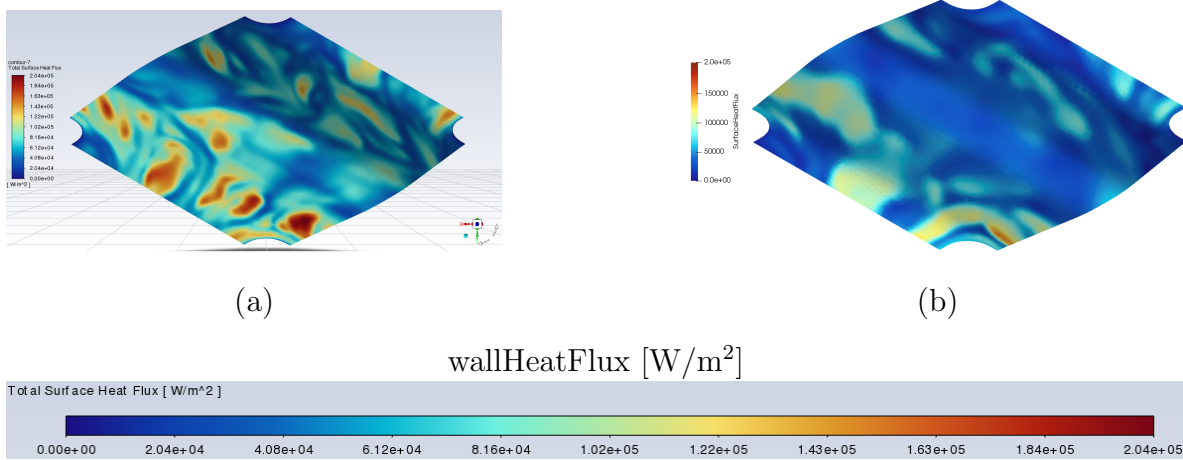
(a)　　　　　　　　　　　　　　　　(b)

wallHeatFlux [W/m²]

Figure 23: Instantaneous surface heat flux stress of the upper plate for the unit cell (left) and the full plate (right).

(a)　　　　　　　　　　　　　　　　(b)
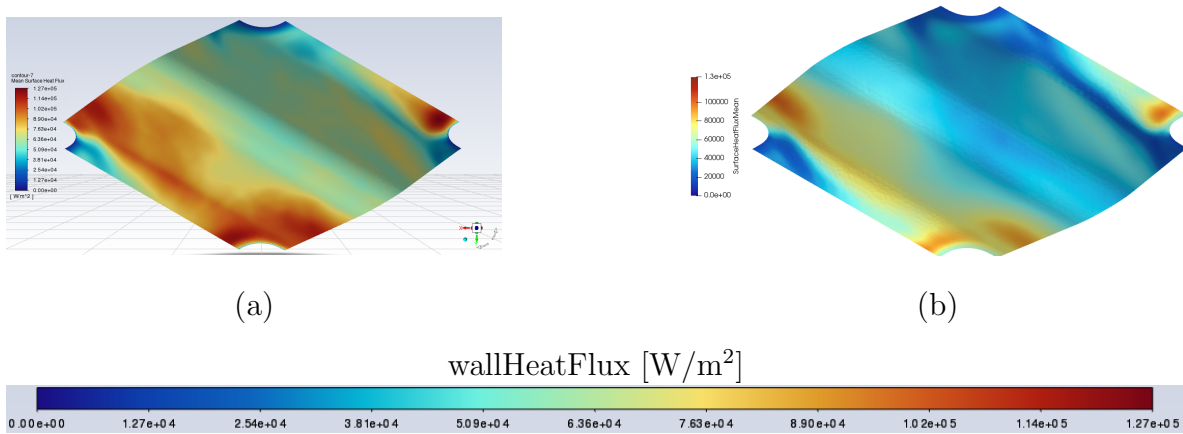
wallHeatFlux [W/m²]

Figure 24: Mean surface heat flux stress of the upper plate for the unit cell (left) and the full plate (right).

The overall contours of the wall shear stress agrees with the benchmark (see fig.22) showing high shear stresses around the sides of the contact points and a streak of high shear along the front side of the corrugation. This seems reasonable since the velocities around the contact points are high and the flow is impinging where the corrugation is contracting. In contrast, low shear stresses are captured in the wake region, at the stagnation point and on the back-side of the corrugation where the velocities are low. When looking at the instantaneous heat flux it looks like the dynamics is captured but more pronounced similar to what was observed for the fluctuating velocity (see fig.23). The mean heat flux captures the high thermal spot in front and to the sides of the contact point a and the streaks of high heat flux mainly on the front-side of the corrugation (see fig.24). Interestingly, it appears that the mean heat flux is much more diffusive for the unit cell which is not really seen for the velocity and wall shear stress.

Perhaps this indicates that the discretization schemes for the velocity and pressure are managing to preserve sharper gradients while the second order upwind scheme for the energy equation is too diffusive. It is expected that the schemes are implemented in a conservative or diffusive way because it is a commercial software that perhaps would be biased towards providing convergence more easily at the cost of accuracy.

4.1.3   Probe Velocity & Temperature Profiles

The velocity profile from top to bottom plate in the middle of the unit cell is presented in figure 26. Similar profile for the temperature through half the channel height is shown in figure 27.
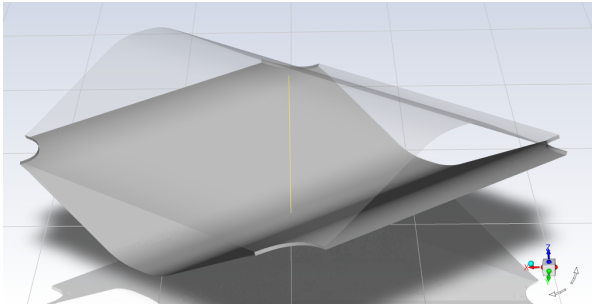

Figure 25: The vertical probe going from top to bottom plate in the middle of the unit cell is shown in yellow.
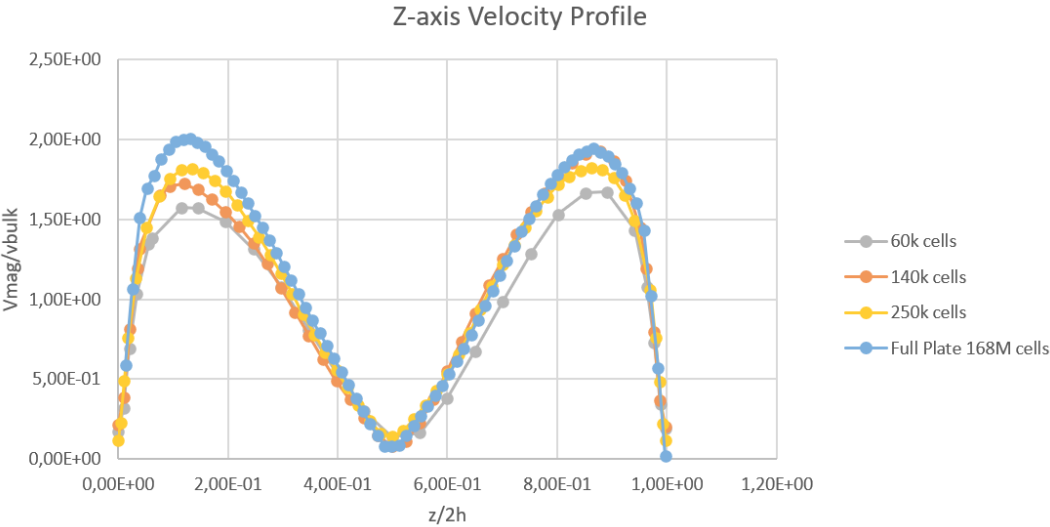

Figure 26: Velocity profile along the vertical probe line displayed in figure 25. The data from the unit cell is plotted for meshes 60k (grey), 140k (orange) and 250k (yellow) and the full plate data is plotted in blue. The velocity magnitude is normalized by the bulk velocity and the height (z) is normalized with the total channel height 2h.

36

From the velocity profile taken from the probe (see fig.25) it can be seen that there is an asymmetry between the velocity peaks for the full plate and the medium and course mesh of the unit cell while the finest mesh is seemingly symmetrical. The asymmetry of the full plate is probably due to it only having heat transfer on one of the plates, instead of both as done with the unit cell, which would cause higher velocities on the hot plate side. It is possible that the asymmetry of the coarser meshes of the unit cell could be due to the fact that all sampling simulations where initialized based on a previous solution of the finest mesh. In doing so the finest mesh will have been simulated for a longer total time even though the sampling time is the same meaning that the flow perhaps is fully developed while it might not be yet for the coarser meshes which could explain the asymmetry. However due to limitations in computational time the cases could not be simulated enough to verify this. Additionally the asymmetry would perhaps disappear if two pressure gradients along the corrugations where set instead of one since this would ensure that the flow had equal driving forces in both directions. Lastly, the peak velocity of the coarsest mesh is a bit lower compared to the other two meshes which are closer which is probably due to a more diffusion caused by the coarser mesh.
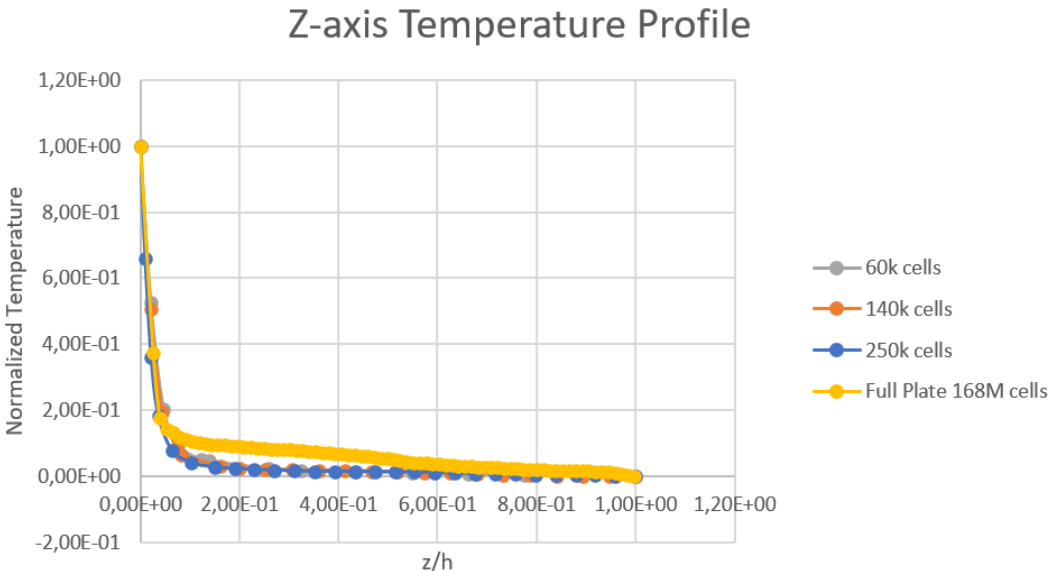

Figure 27: Temperature profile along the vertical probe line displayed in figure 25. The data from the unit cell is plotted for meshes 60k (grey), 140k (orange) and 250k (yellow) and the full plate data is plotted in blue. The temperature is normalized to be equal to one at the wall and zero in the middle of the channel.

In figure 27 the normalized temperature profile is shown for the full plate and the three meshes along the same probe as the velocity profile. Note that only half of the probe length is used here. Therefore the mean channel height h is used to normalize the height

(z) so that it is equal to zero at the wall and one in the middle of the channel. The profile looks to be consistent for the three meshes. The full plate seems to get a thicker thermal boundary layer which could be because the wall treatments are different in OpenFoam compared to Fluent.

4.1.4 Darcy Friction Factor and Nu/Pr$^{1/3}$

Experimental as well as full plate data for Darcy Friction Factor and Nu/Pr$^{1/3}$ is plotted against the unit cell results in fig.28 and fig.29 respectively.
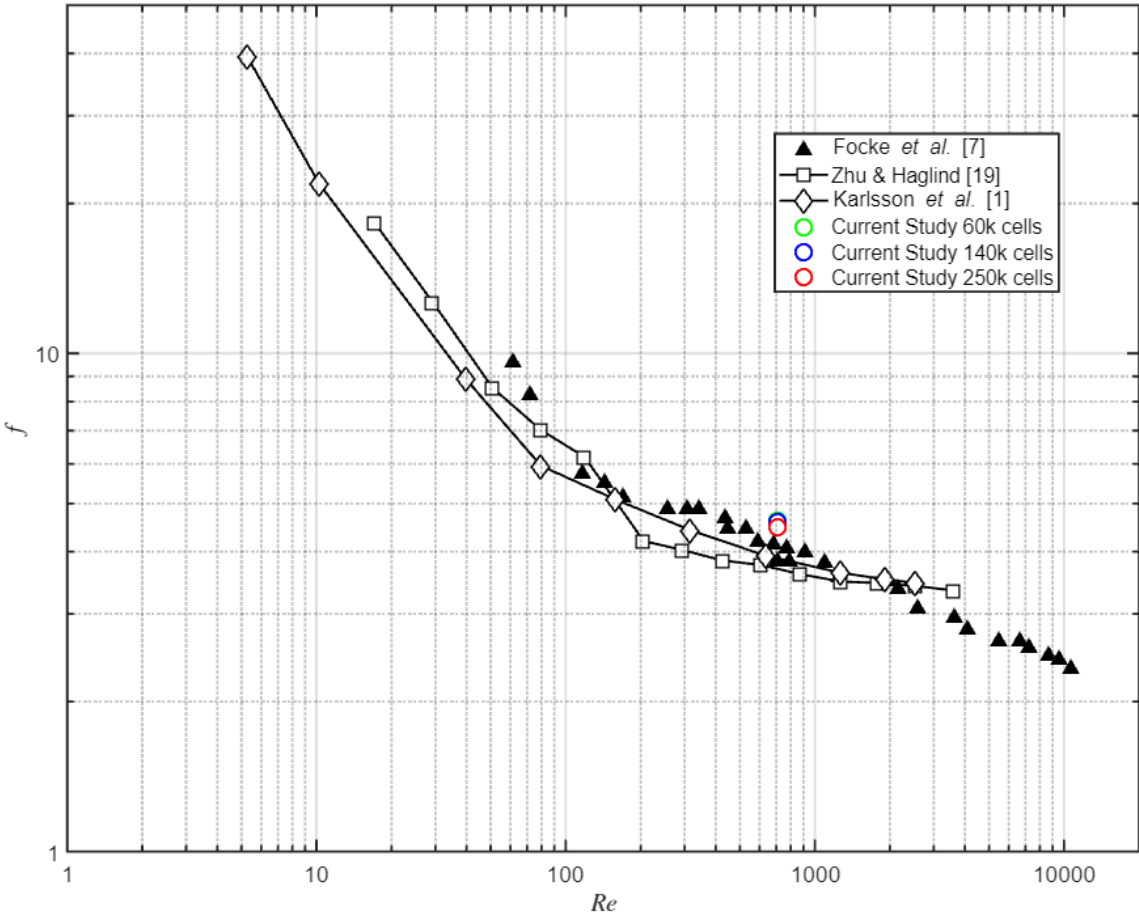

Figure 28: The Darcy friction factor of the unit cell with the three available meshes are plotted for the Reynolds number 841 (circles) in a log-log scale. Results of the full plate (Karlsson et al. [1] and Focke et al. [7]) as well as the unit cell of Zhu & Haglind [19] are also plotted for a wide range of Reynolds number to provide context.
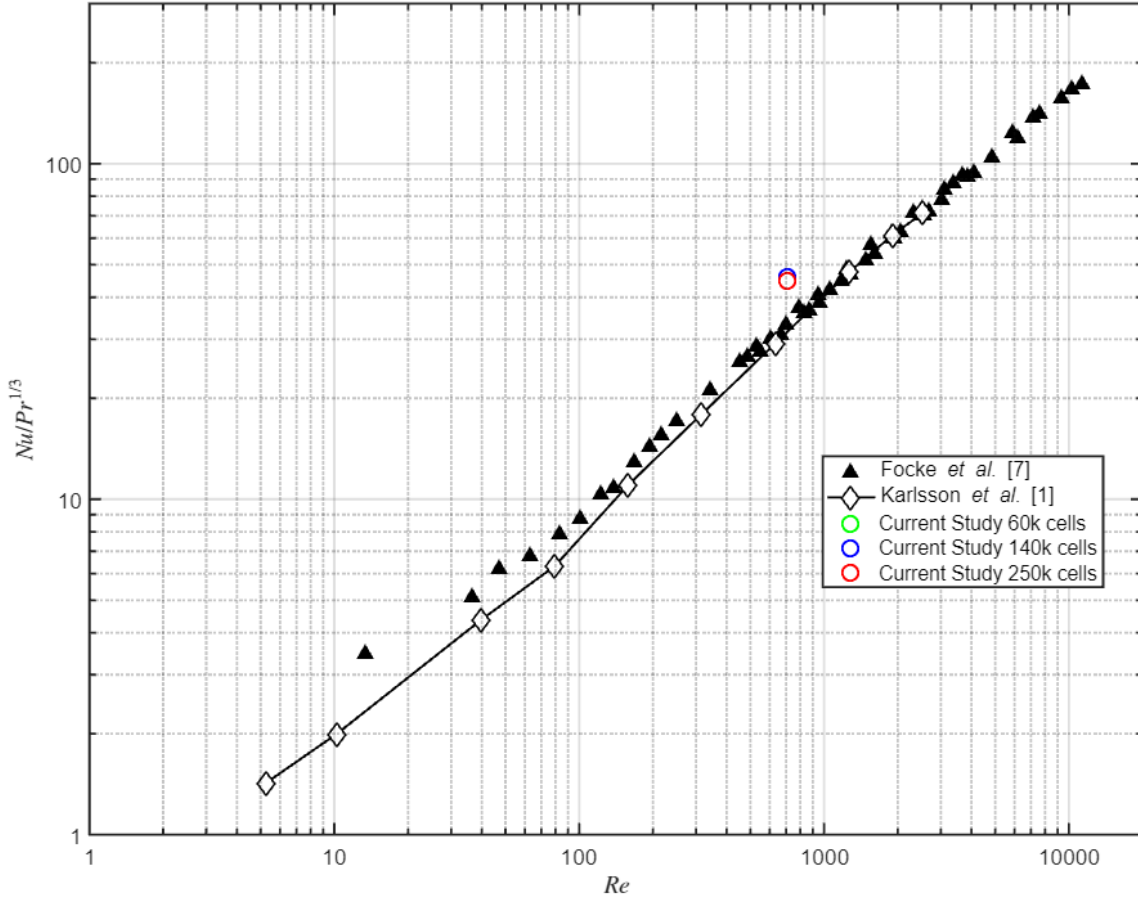
38

Figure 29: The average $Nu/Pr^{1/3}$ over the two walls of the unit cell is plotted for the Reynolds number 841 (circles) in a log-log scale. The values are taken from results of the three meshes. Additionally, results of the full plate (Karlsson et al. [1] and Focke et al. [7]) are plotted for different Reynolds number to give context.

Table 7: Percentage difference of Darcy friction factor f and $Nu/Pr^{1/3}$ for the three mesh sizes when comparing with experimental data from Focke et al. [7].

Re = 841

Number	Mesh60k	Mesh140k	Mesh250k	Focke exp.
f	4.64	4.6	4.48	3.92
Δ	19.0 %	18.0 %	14.9 %	-
$Nu/Pr^{1/3}$	45.7	46.1	45.1	36.1
Δ	26.4 %	27.5 %	24.7 %	-

The global flow and heat transfer evaluation of the unit cell shows that both the Darcy friction factor and the $Pr^{1/3}$ normalized Nusselts number for the three meshes are close to a eachother relative to the spread of data from the benchmark [1] and experiments [7]

39

for different Reynolds numbers (see fig.29 and fig.28). However when looking at table 7 it can be seen that the Darcy friction factor and the $Nu/Pr^{1/3}$ for finest mesh are overpredicted by by 14.9 and 24.7 percent respectively when comparing with the experimental data.

To summarize the results of the unit cell when comparing with the full plate, the global evaluation parameters Darcy Friction Factor and $Nu/Pr^{1/3}$ are overpredicted. These are relevant parameters since they can be used to evaluate performance of PHE:s with regards to overall heat transfer and flow losses. The fact that they are both overpredicted is consistent with the results of the velocity field where it was shown that instantaneous and mean velocity agree somewhat whereas the fluctuations of the velocity are largely overpredicted. Higher fluctuations in velocity indicates higher turbulence which could explain the overprediction of the heat transfer and flow losses.

Why the turbulence is overpredicted could be because the periodic feedback loop somehow allows it the build up too much or perhaps the wall treatment overpredicting the strain rates and therefore the production of turbulence. A counter argument to this is that the periodic implementation would be expected to preserve the total energy going into the system.

The discrepancy in results could also be due to the sub-optimal boundary conditions where the pressure gradient is not aligned with the periodic directions and the periodic heat transfer for convective boundary condition being unknown in the software (Fluent). However, the results show that the overall dynamics and characteristics, when looking at instantaneous and mean quantities, are well captured which suggests that the boundary conditions are able to reproduce the larger scale physics. Perhaps it is the smaller scale physics that are the root cause of the problem which are more dependent on how the modeling and numerics are done.

Moreover, the overall flow in terms of velocity, wall shear stress, and Darcy friction factor seem to agree better than the heat transfer in terms of surface heat flux, temperature profile and $Nu/Pr^{1/3}$. It was for example observed that the wall heat flux was more diffusive than the wall shear stress which could be due to the discritezation of the energy equation being too diffusive. Or it could be due to the different wall treatment used in OpenFoam and Fluent where the thermal boundary layer is thinner than expected which supports the overprediction of the heat transfer.

Another reason that the heat transfer is further from the experimental and benchmark data compared to the Darcy friction factor is perhaps because it is more sensitive

to deviations in Reynolds number or turbulence. It can be seen from the slope around Reynolds number used (841) in figure 29 and figure 28 that it is steeper for the $\mathrm{Nu/Pr}^{1/3}$ number compared to the friction factor which supports that the heat transfer is more sensitive to the predicted turbulence.

One final possibility is that the turbulence is not overpredicted but instead the calculated Reynolds number is lower than the actual one since it is calculated based on the bulk velocity which is taken from a slice in the middle of the unit cell normal to the main flow direction. If the current method of obtaining the bulk velocity is faulty it will give the wrong Re number and thus another level of turbulence as a consequence. However when comparing the unit cell results of Re 841 to the full plate of a higher Re 1273 the full plate the fluctuating velocity component is still higher for the unit cell even though the instantaneous and mean velocities are much lower. This shows that it is in fact the fluctuations of the velocity which are overpredicted in relation to the mean and instantaneous velocity.

4.2 Mesh Resolution and Model Comparisons

4.2.1 LES Meshes

Mean and instantaneous velocity fields taken from a slice at half the total channel height for the three meshes using LES are shown in fig.
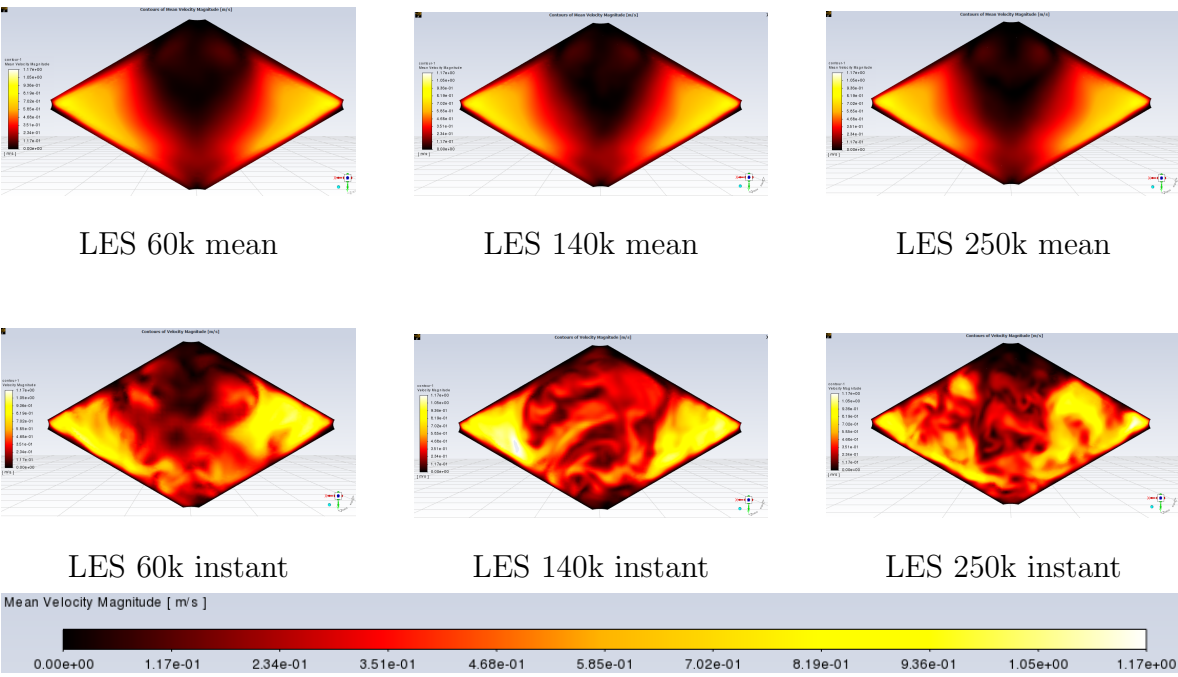

| LES 60k mean | LES 140k mean | LES 250k mean |

| LES 60k instant | LES 140k instant | LES 250k instant |

Figure 30: Mean (upper) and instantaneous (lower) velocity fields are shown from the coarsest 60k mesh (left) to the finest 250k mesh (right).

4.2.2 RANS vs URANS

Results of the velocity fields in a plane taken at the mean channel height for RANS and URANS (see fig.31).

(a) RANS 140k

(b) RANS 250k

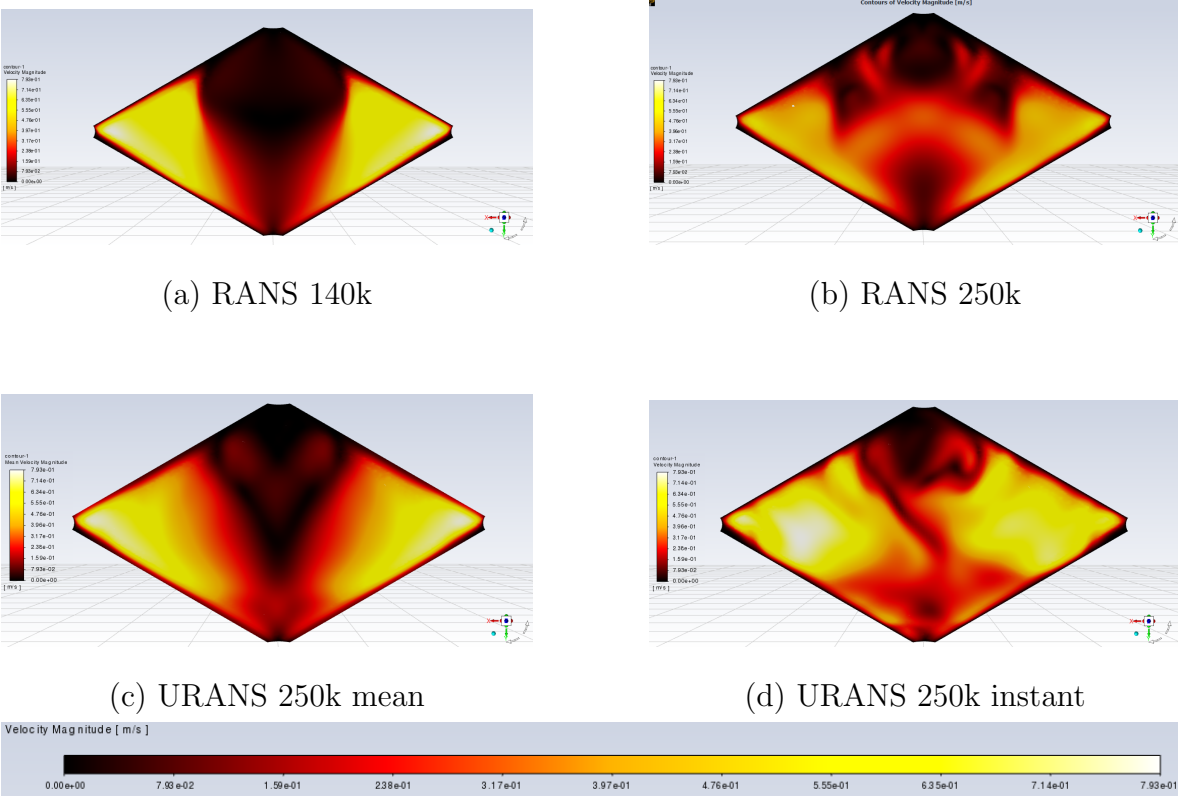(c) URANS 250k mean

(d) URANS 250k instant

Figure 31: RANS velocity contours for the 140k cell (a) and 250k cell (b) mesh respectively. URANS with the fine 250k cell mesh is shown in terms of mean velocity (c) and instantaneous velocity (d).

When running steady state RANS it turns out that the finest mesh of 250k cells did not converge while the lower mesh resolutions did. When comparing the velocity fields of the finest and medium mesh it seems like the medium mesh displays a smooth contour (see fig.31) similar to the one obtained from the LES simulation (see fig.18). In contrast, the finest mesh shows a less smooth contour with nonphysical velocity branches that are not observed in the LES results (see fig.31). This indicates that the finest mesh is too fine for the RANS solution to converge where appears to attempt to solve finer structures that does not exist.

4.2.3 URANS vs LES

URANS and LES simulations shown for the fine 250k cell mesh in terms of wall shear stress and surface heat flux in figures 32-33 and figures 34-35 respectively.
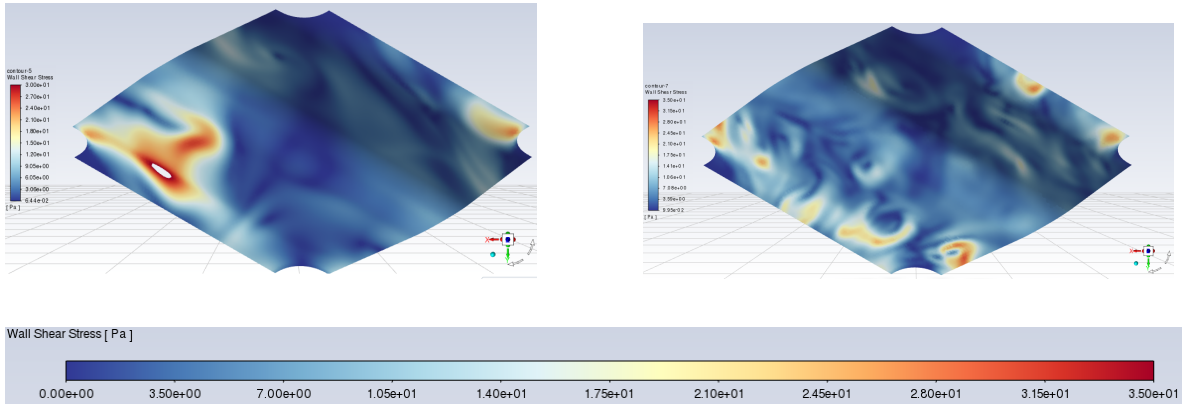

Figure 32: Instantaneous wall shear stress contour for URANS (left) and LES (right).
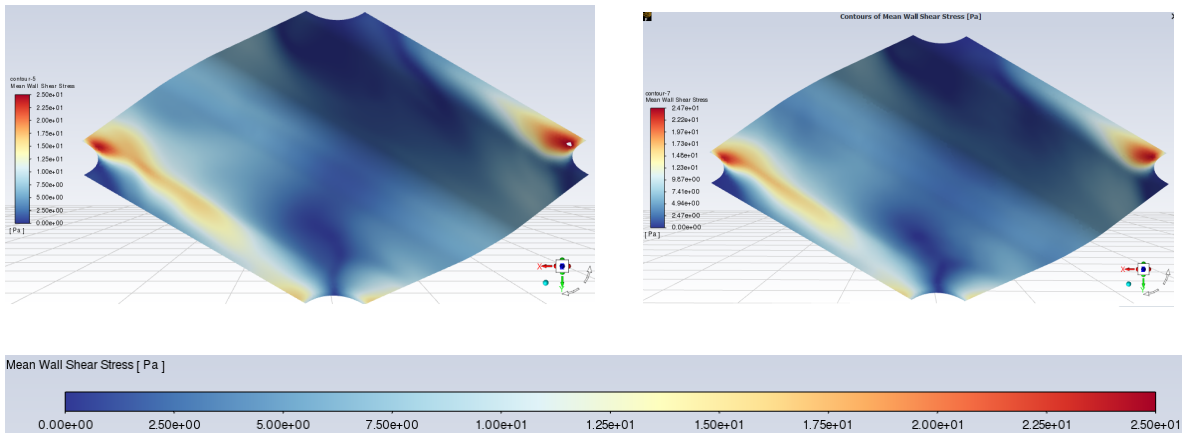

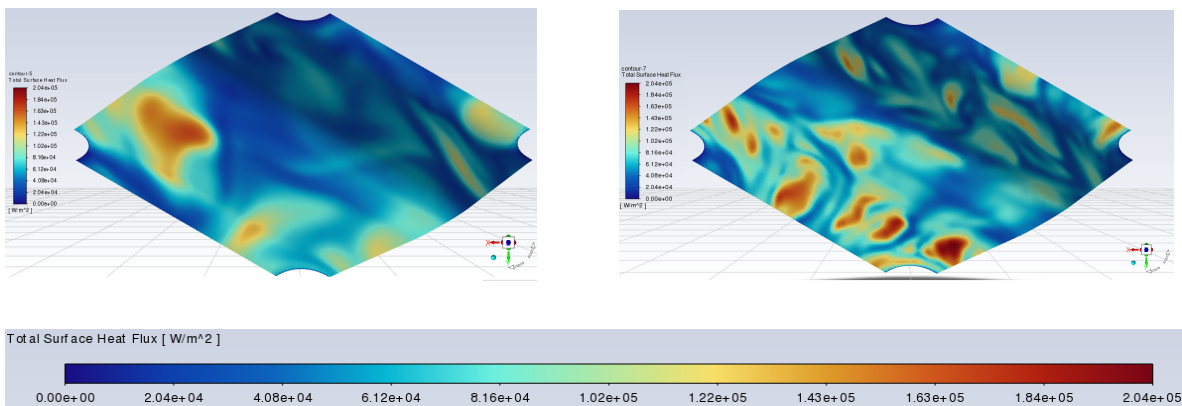Figure 33: Mean wall shear stress contour for URANS (left) and LES (right).

Figure 34: Instantaneous wall heat flux contour for URANS (left) and LES (right).
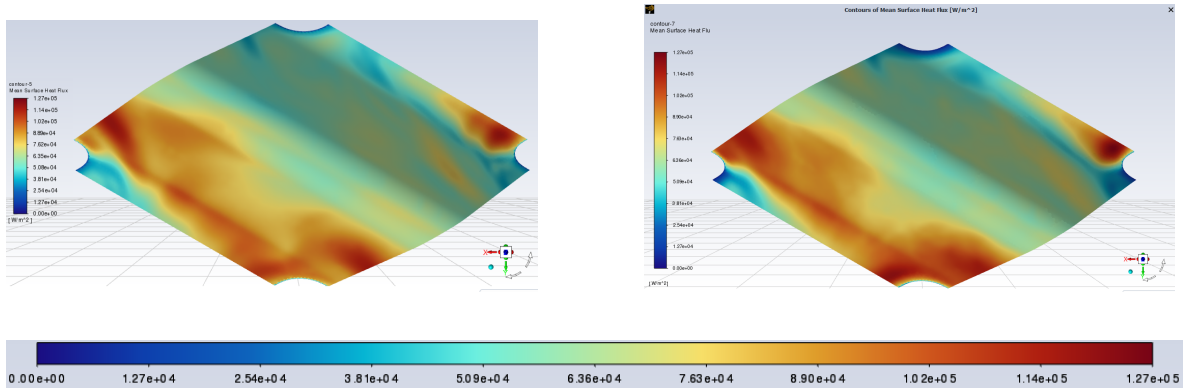
Figure 35: Mean wall heat flux contour for URANS (left) and LES (right).

Comparing the heat flux and wall shear stress contours for URANS and LES of the unit cell there is clearly more dynamic turbulence in the LES results for the instantaneous values (see fig.34 and fig.32). The mean values look similar with URANS having slightly higher shear stress peak values (see fig.35 and fig.33).

4.3 Lumley Triangle

Here the invariants ξ and η of the Reynolds stress anisotropy tensor (see subsection 2.12) are plotted in the Lumley triangle to visualize the anisotropic turbulence and its components of the flow.
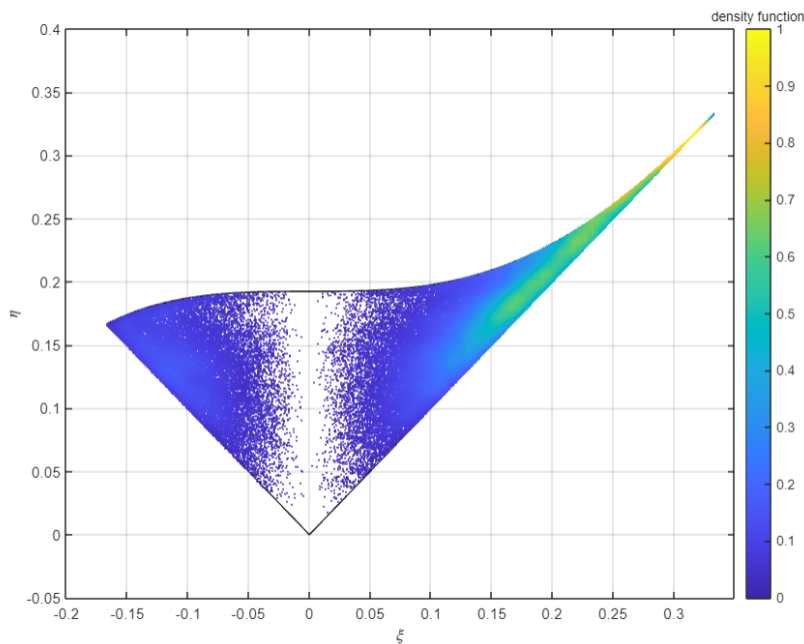

Figure 36: The different turbulence components for the unit cell are plotted in the Lumley triangle. A colormap ranging from one to zero shows how often each component occurs where higher values indicate more frequent occurrence.

44

The Lumley triangle seem reasonable showing axisymmetric prolate and 1-component anisotropic turbulence which is similar to a canonical channel flow (see fig.36 and fig.9) [20]. There is also almost no isotropic turbulence which is expected due to the high strain rates caused by the complex plate geometry.

4.4 Wake

Figure 37 is a contour of the dynamic pressure which illustrates the instantaneous wake and stagnation point behind and in front of the contact point respectively where the velocity and thus dynamic pressure are low.
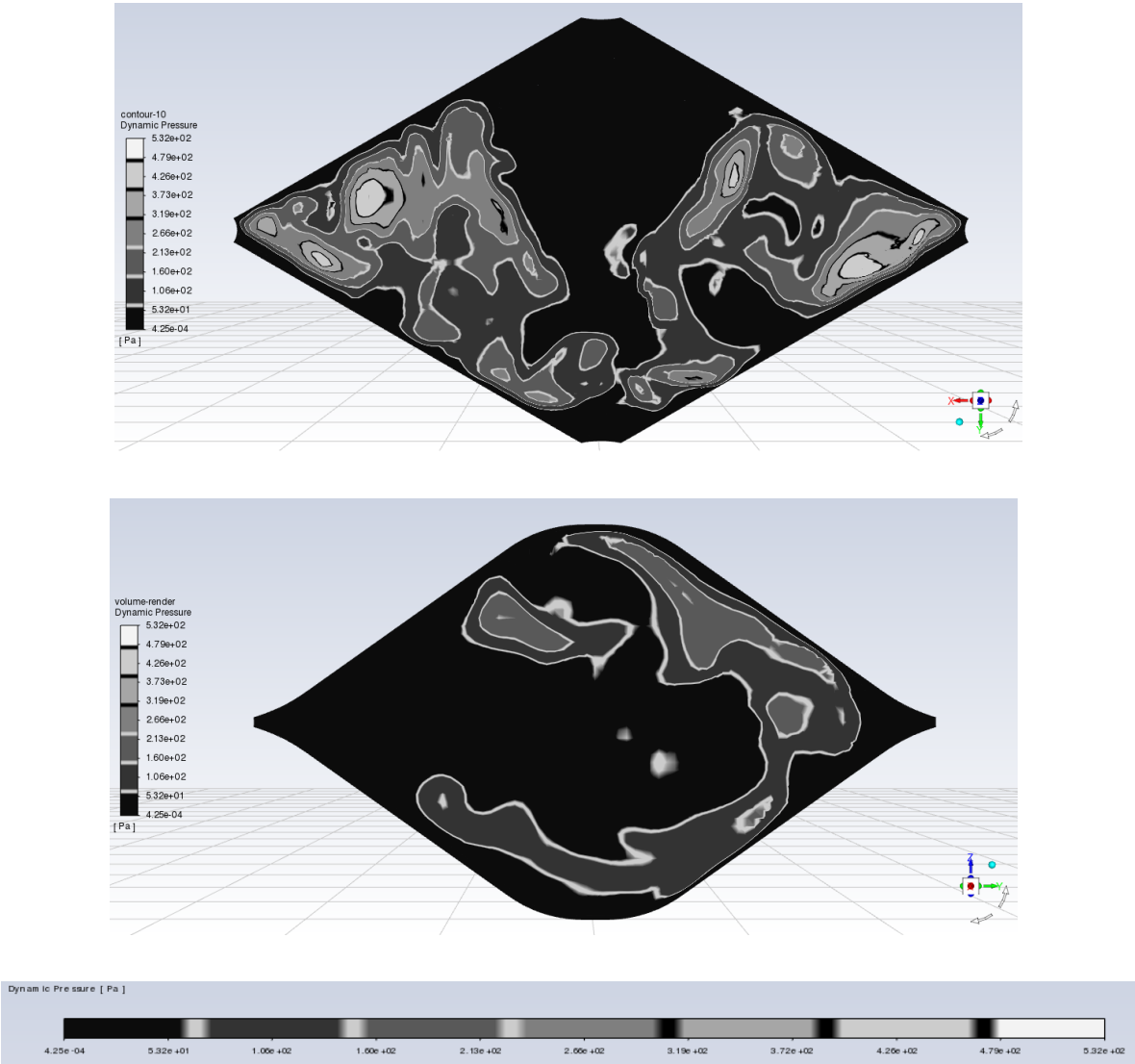
Figure 37: Instantaneous dynamic pressure of a slice taken at the mean channel height (upper) and a slice between the front and back contact points normal to the spanwise direction (lower).

4.5 Vortex Structures

The high heat flux in front of the contact point from figure 38 seems to arise from a horseshoe vortex that makes the thermal boundary layer thinner which was discovered in the benchmark article [1].

Figure 38: Iso-surfaces of the Q-criterion illustrating vortex core structures and instantaneous wall heat flux.

4.6   Sources of Errors

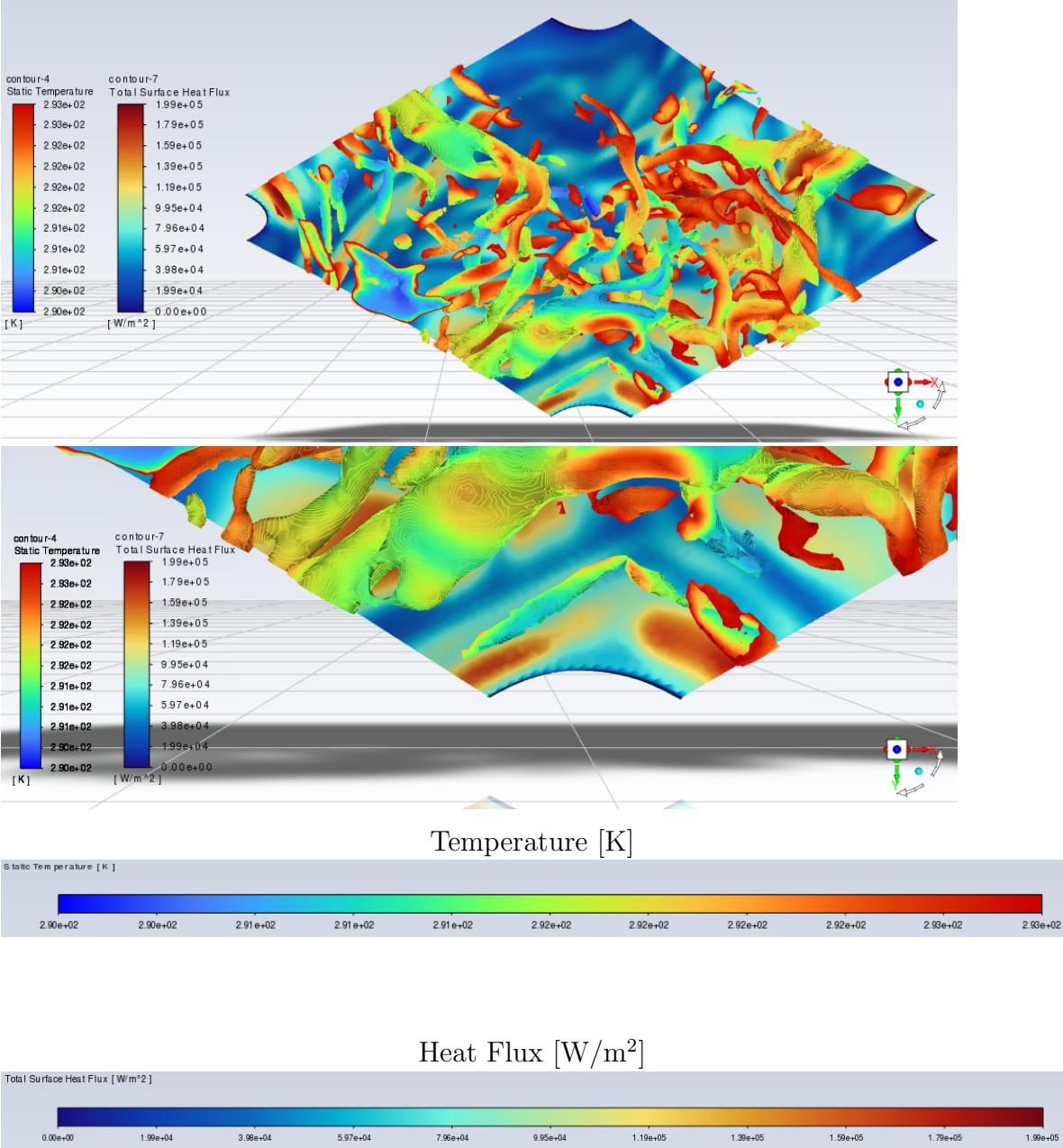The discretized equations might be too diffusive causing inaccurate results. For example the bounded central differencing scheme could switch to lower order schemes such as first order upwind to preserve stability of the solution without the user knowing.

The benchmark solely simulates one set of plate channels only one plate has heat transfer. Meanwhile the heat transfer on the other plate is disregarded to mitigate the discrepancy of having inlet and outlet ducts on that side. This causes a skewed temperature distribution since the distance along which the fluid is heated by the wall is no longer independent of the path it takes. In contrast, the skewness effect is not taken into account in the unit cell and both top and bottom plates contribute to the heat transfer. The two-sided heat transfer is used because this is how the method is going to be used in the future since it is closer to how it is inside a real PHE. This might cause a difference when comparing the heat transfer of the unit cell to the full plate and is thus two sources of errors. However it is assumed that the heat transfer coefficients of the evaluated plate would not be significantly affected by the adiabatic plate of the benchmark. Furthermore, the skewness of the temperature field is assumed to alter the global heat transfer coefficients negligibly.

The implementation of the periodic boundary conditions for the flow and heat transfer in Fluent is an uncertainty and could cause errors in the results and explain why the mesh sensitivity study did not converge. To begin with, the fixed pressure gradient condition applied to drive the correct mass flow can only be set in one direction in Fluent. Ideally the pressure gradient would be fixed in the two periodic directions i.e. along the corrugations. Secondly, the fluent user guide recommends constant wall heat flux or temperature for periodic flow. However in order to resemble the benchmark convective boundary conditions were used which means that how the heat transfer is solved can only be speculated (see subsection 3.1) since the implementation is confidential.

The heat transfer and Darcy friction factor should be greatly affected by the thermal and momentum boundary layer. The corrugation causes a complex behaviour by thinning, separation and reattachment of the boundary layers. If these phenomenons are not captured consistently it could explain the discrepancy in heat transfer and friction factors between the unit cell and the full plate simulations. The benchmark and the unit cell model the wall differently due to the different software which means the near wall behaviour is treated differently and could explain the differences observed in the results. This might also explain the difference in fluctuating velocity, since if the dampening of the local eddy viscosity near the wall is underpredicted or the strain rate is overpredicted the turbulence could be underdamped or its production could be too high.

One last source of error is typically in OpenFoam a turbulent Prandtl number is used to model the subgrid turbulent heat transfer whereas in fluent an additional wall turbulent Prandtl number is used which seems to be used in the wall modeling which could affect the heat transfer near the wall.

5   Conclusion and Future Work

A method for doing LES of a unit cell of PHE:s have been developed. The results have been compared to simulations of a full plate in order to evaluate the accuracy and level of detail.

5.1   Advantages

Using the current unit cell setup a reduction in computational cost is obtained since the computational domain is many times smaller and the setup has the potential to become very cheap. This can enable LES simulations to be done within a reasonable time compared to the full plate method. Being able to use LES will give a more accurate and detailed insight into the flow behaviour and heat transfer mechanisms. This could be a great tool for researching and developing future plate patterns and textures at Alfa Laval. Additionally, the reduced simulation time could be useful when for example iterating and comparing many different design parameters approximately.

5.2   Disadvantages

Some information is lost where inlet, outlet and side wall interactions are disregarded. However, the results of the large-scale physics seem to agree with the full plate which is a good sign that this assumption is reasonable. Additionally, larger plates with more contact points than the benchmark plate which is relatively small should lose less information since the assumption of fully developed flow would hold over a larger portion of the plate. The same goes for high theta since the spanwise distribution of the flow will be more evenly distributed. The periodic domain will constrict information to ta travel with a wavelength equal to the periodic length of the unit cell at maximum for steady state simulations while transient simulations could perhaps capture longer wavelengths than the periodic length by solving a cyclic time evolution.

5.3   Future Work

It would be a good idea to investigate whether some of the resulting discrepancies mainly come from the differences between OpenFOAM and Fluent or the unit cell and

full plate approach or if it is a combination of both. Therefore a more direct comparison should be made between the two methods using either Fluent or OpenFoam for both cases.

Optimize the computational cost of the current unit cell setup used in Fluent in order to run more simulations at a reasonable time. Once this is done a wall treatment study for different y^+ values can be done to see if this is a contributing factor to the overpredictions discussed. Also trying different subgrid models would be a good idea to see if there is a substantial sensitivity between the models contributing to the current deviation in results.

Do a Reynolds number sweep to see if the friction factor and Nusselt Prandtl numbers obtain to see if there is a systematic deviation from the benchmark results.

Try unit cells with different numbers of contact points to see how the prediction of the heat transfer and flow resistance changes with increased periodic domain size. However, with the current meshing tool the periodic faces will have to be cut at an angle for the face mapping to work as previously discussed (see subsection 3.1). It would be good to instead use unit cells with faces normal and tangential to the mean flow direction to align the pressure gradient with the periodic direction which has the added benefit of simplifying how to define the flow and heat transfer numbers. For example the five contact point cell with another meshing program like Ansys meshing could be done to better align the periodic faces.

Once the single channel unit cell is well understood and tested, the next step could be to try conjugate heat transfer which would be a more expensive but realistic boundary condition. Then heat transfer between two different fluids could be analysed.

5.4   Summary

To sum up, creating a unit cell geometry and setting up the boundary conditions according to subsection 3.4 can be a bit tricky at first but is a pretty short and simple process after it's been done once. Moreover, the unit cell method seems to capture the large-scale physics and flow characteristics indicating that the boundary conditions are somewhat appropriate which is promising. Furthermore, it could be a good idea to align the pressure gradient with the periodic directions as this could improve the results. The smaller-scale physics, turbulence and heat transfer are overpredicted by a significant amount indicating that the method needs to be refined with regards to the more intricate modeling and numerics. Before investigating the modeling and numerics

which can be time consuming and require a lot of simulation runs it is recommended that the simulation time of the current setup is optimized as the computational cost is unreasonably excessive relative to how small the computational domain is. The computational cost could probably be immensely reduced compared to the current one after optimization. If these things are resolved the method has a great potential to be a simple case to set up that drastically reduces the computational cost while providing detailed and accurate results using LES.

References

[1] G. Karlsson, C. Fureby, L. Wang, C. Norberg, M. Holm, and F. Strömer, "Numerical study of heat transfer , flow fields, turbulent length scales and anisotropy in corrugated heat exchanger channels," *Phys. Fluids*, vol. 34, 055123 (2022).

[2] Alfa Laval, "Alfa laval in brief – who we are and what we do," Available at https://www.alfalaval.com/about-us/our-company (2023/04/17).

[3] Alfa Laval, "5 reasons to use plate-and-frame heat exchangers instead of shell-and-tube," Available at https://www.alfalaval.se/microsites/packningsforsedda-plattvarmevaxlare/verktyg/packningsforsedda-plattvarmevaxlare-jamfort-med-tubvarmevaxlare/ (accessed: 2023/04/19).

[4] H. K. Versteeg and W. Malalasekera, *An Introduction to Computational Fluid Dynamics: The Finite Volume Method*, 2nd ed. Pearson Education Limited, 2007.

[5] S. B. Pope, *Turbulent Flows*. Cambridge University Press, 2000.

[6] ANSYS Inc, "Ansys fluent 12.0 theory guide," Available at https://www.afs.enea.it/project/neptunius/docs/fluent/html/th/main_pre.htm (2009/01/23).

[7] W. W. Focke, J. Zachariades, and I. Olivier, "The effect of the corrugation inclination angle on the thermohydraulic performance of plate heat exchangers," *Int. J. Hear Mass Transfer*, vol. 28, no. 8, pp. 1469–1479, 1985.

[8] Alfa Laval, "How gasketed plate heat exchangers work," Available at https://www.alfalaval.se/microsites/packningsforsedda-plattvarmevaxlare/verktyg/hur-packningsforsedda-plattvarmevaxlare-fungerar/ (accessed: 2023/04/14).

[9] Alfa Laval, "Plate technology," Available at https://www.alfalaval.se/microsites/packningsforsedda-plattvarmevaxlare/verktyg/platt-teknik/ (accessed: 2023/04/14).

[10] Alfa Laval, "Plate heat exchanger calculation method," https://www.alfalaval.se/microsites/packningsforsedda-plattvarmevaxlare/verktyg/berakningsmetod/ (accessed: 2023/09/02).

[11] R. Yu and C. Fureby, "AdvancedCFD_2022_lecture," Available at https://canvas.education.lu.se/courses/17406/assignments/104175?module_item_id=607465 (2022).

[12] W. K. Anderson and D. L. Bonhaus, "An implicit upwind algorithm for computing turbulent flows on unstructured grids," *Computers & Fluids*, vol. 23, no. 1, pp. 1–21, 1994.

[13] B. P. Leonard, "The ultimate conservative difference scheme applied to unsteady one-dimensional advection," *Computer Methods in Applied Mechanics and Engineering*, vol. 88, no. 1, pp. 17–74, 1991.

[14] R. Issa, "Solution of the implicitly discretised fluid flow equations by operator-splitting," *Journal of computational physics*, vol. 62, no. 1, pp. 40–65, 1986.

[15] Y. Gao and Y. Liu, "Investigation of the unsteady flow features in a tip leakage flow model using large-eddy simulation," Proceedings of Global Power and Propulsion Society, presented at the Beijing Conference 2019 16th – 18th September, Available at https://gpps.global/wp-content/uploads/2021/02/GPPS-BJ-2019_paper_181.pdf (accessed: 2023/05/13).

[16] J. Zhan, Y. Li, W. O. Wai, and W. Hu, "Comparison between the Q criterion and rortex in the application of an in-stream structure," *Physics of Fluids*, vol. 31, 2019.

[17] F. Nicoud and F. Ducros, "Subgrid-scale stress modelling based on the square of the velocity gradient tensor," *Flow, Turbulence and Combustion*, 1999.

[18] M. Ciofalo, J. Stasiek, and M. W. Collins, "Investigation of flow and heat transfer in corrugated passages-II numerical simulations," *Int. J. Heat Mass Transfer*, vol. 39, no. 2, pp. 165–192, 1996.

[19] X. Zhu and F. Haglind, "Relationship between inclination angle and friction factor of chevron-type plate heat exchangers," *International Journal of Heat and Mass Transfer*, vol. 162, no. 2, 2020.

[20] R. Poletto, A. Revell, T. Craft, and N. Ashton, "Embedded DDES of 2D hump flow," in Proc. of the 4th Hybrid RANS-LES symposium Conf. on Notes on Numerical Fluid Mechanics and Multidisciplinary Design 117, September 2012, Beijing. Available at: https://www.researchgate.net/publication/260991511_Embedded_DDES_of_2D_hump_flow (accessed: 2023/06/01).